

1 **Title: Multivalency transforms SARS-CoV-2 antibodies into broad and ultrapotent**
2 **neutralizers**

3
4
5 Edurne Rujas^{1,2,3}, Iga Kucharska¹, Yong Zi Tan¹, Samir Benlekbir¹, Hong Cui¹, Tiantian Zhao⁴,
6 Gregory A. Wasney^{1,5}, Patrick Budylowski^{6,7}, Furkan Guvenc^{6,8}, Jocelyn C. Newton¹, Taylor
7 Sicard^{1,2}, Anthony Semesi¹, Krithika Muthuraman¹, Amy Nouanesengsy^{1,2}, Katherine Prieto¹,
8 Stephanie A. Bueler¹, Sawsan Youssef⁹, Sindy Liao-Chan⁹, Jacob Glanville⁹, Natasha Christie-
9 Holmes⁶, Samira Mubareka^{10,11}, Scott D. Gray-Owen⁸, John L. Rubinstein^{1,2,12}, Bebhinn
10 Treanor^{4,13,14}, Jean-Philippe Julien^{1,2,4}

11
12 **Affiliations:**

13 ¹ Program in Molecular Medicine, The Hospital for Sick Children Research Institute, Toronto, ON,
14 Canada.

15 ² Department of Biochemistry, University of Toronto, Toronto, ON, Canada.

16 ³ Biofisika Institute (CSIC, UPV/EHU) and Department of Biochemistry and Molecular Biology,
17 University of the Basque Country (UPV/EHU), Bilbao, Spain.

18 ⁴ Department of Immunology, University of Toronto, Toronto, ON, Canada.

19 ⁵ The Structural & Biophysical Core Facility, The Hospital for Sick Children Research Institute,
20 Toronto, ON, Canada

21 ⁶ Combined Containment Level 3 Unit, University of Toronto, Toronto, ON, Canada.

22 ⁷ Institute of Medical Science, University of Toronto, Toronto, ON, Canada.

23 ⁸ Department of Molecular Genetics, University of Toronto, ON, Canada.

24 ⁹ Distributed Bio, South San Francisco, CA, United States.

25 ¹⁰ Department of Laboratory Medicine and Pathobiology, University of Toronto, Toronto, ON,

26 Canada.

27 ¹¹ Sunnybrook Health Sciences Centre, Toronto, ON, Canada.

28 ¹² Department of Medical Biophysics, University of Toronto, Toronto, ON, Canada.

29 ¹³ Department of Cell and Systems Biology, University of Toronto, ON, Canada.

30 ¹⁴ Department of Biological Sciences, University of Toronto Scarborough, Toronto, ON, Canada.

31 *Correspondence should be addressed to: jean-philippe.julien@sickkids.ca

32

33

34

35

36

37

38

39

40

41

42

43 **Abstract**

44 The novel severe acute respiratory syndrome coronavirus 2 (SARS-CoV-2), which causes
45 Coronavirus Disease 2019 (COVID-19), has caused a global pandemic. Antibodies are powerful
46 biotherapeutics to fight viral infections; however, discovery of the most potent and broadly acting
47 clones can be lengthy. Here, we used the human apoferritin protomer as a modular subunit to drive
48 oligomerization of antibody fragments and transform antibodies targeting SARS-CoV-2 into
49 exceptionally potent neutralizers. Using this platform, half-maximal inhibitory concentration
50 (IC_{50}) values as low as 9×10^{-14} M were achieved as a result of up to 10,000-fold potency
51 enhancements. Combination of three different antibody specificities and the fragment
52 crystallizable (Fc) domain on a single multivalent molecule conferred the ability to overcome viral
53 sequence variability together with outstanding potency and Ig-like *in vivo* bioavailability. This
54 MULTi-specific, multi-Affinity antiBODY (Multobody; or MB) platform contributes a new class
55 of medical countermeasures against COVID-19 and an efficient approach to rapidly deploy potent
56 and broadly-acting therapeutics against infectious diseases of global health importance.

57

58 **One Sentence Summary:** multimerization platform transforms antibodies emerging from
59 discovery screens into potent neutralizers that can overcome SARS-CoV-2 sequence diversity.

60

61

62

63

64 **Introduction**

65 The continuous threat to public health from respiratory viruses such as the novel SARS-CoV-2
66 underscores the urgent need to rapidly develop and deploy prophylactic and therapeutic
67 interventions to combat pandemics. Monoclonal antibodies (mAbs) have been used effectively for
68 the treatment of infectious diseases as exemplified by palivizumab for the prevention of respiratory
69 syncytial virus in high-risk infants¹ or Zmapp, mAb114 and REGN-EB3 for the treatment of
70 Ebola². Consequently, mAbs targeting the Spike (S) protein of SARS-CoV-2 have been a focus
71 for the development of medical countermeasures against COVID-19. To date, several antibodies
72 targeting the S protein have been identified^{3–19} and several are under clinical evaluation^{20,21}.
73 Receptor binding domain (RBD)-directed mAbs that interfere with binding to angiotensin
74 converting enzyme 2 (ACE2), the receptor for cell entry²², are usually associated with high
75 neutralization potencies^{11,12,14}.
76 mAbs can be isolated by B-cell sorting from infected donors, immunized animals or by identifying
77 binders in pre-assembled libraries. Despite these methodologies being robust and reliable for the
78 discovery of virus-specific mAbs, identification of the best antibody clone can be a lengthy
79 process. For example, RNA viruses have a high mutation rate. Indeed, 198 naturally occurring
80 mutations in the S protein of SARS-CoV-2 have been already registered in the GISAID database²³.
81 Identification of broadly neutralizing mAbs (bnAbs) that target the most conserved epitopes to
82 overcome viral escape mutations is therefore critical. This approach has been employed to discover
83 bnAbs against human immune deficiency virus 1 (HIV-1)²⁴, Influenza²⁵, and Ebola²⁶. However,
84 their identification required extensive sampling and high-throughput sequencing and consequently
85 several years of research. Hence, there is an unmet need for the development of a platform that

86 bridges antibody discovery and the rapid identification and deployment of highly potent and
87 broadly neutralizing mAbs.
88 The potency of an antibody is greatly affected by its ability to simultaneously interact multiple
89 times with its epitope²⁷⁻²⁹. This enhanced apparent affinity, known as avidity, has been previously
90 reported to increase the neutralization potency of nanobodies^{30,31} and IgGs over Fabs^{9,16,18} against
91 SARS-CoV-2. In order to rapidly propel mAbs that emerge during initial screening efforts into
92 potent neutralizers against SARS-CoV-2, we have developed an antibody-scaffold technology,
93 using the human apoferritin protomer as a modular subunit, to multimerize antibody fragments.
94 We demonstrate the ability of this technology to combine one to three different Fab specificities
95 together with Fc on the same molecule. The resulting MB molecules can increase mAb potency
96 by up to four orders of magnitude and resist sequence variability in the spike protein. Therefore,
97 the MB offers a versatile “plug-and-play” platform to enhance anti-viral characteristics of
98 prophylactic/therapeutic molecules in the fight against the SARS-CoV-2 pandemic, and to be
99 quickly deployed in the setting of emerging pandemics.

100

101 **Results**

102 **Avidity enhances neutralization potency**

103 We used the self-assembly of the light chain of human apoferritin to multimerize antigen binding
104 moieties targeting the SARS-CoV-2 S glycoprotein. Apoferritin protomers self-assemble into an
105 octahedrally symmetric structure with an ~6 nm hydrodynamic radius (R_h) composed of 24
106 identical polypeptides³². The N terminus of each apoferritin subunit points outwards of the
107 spherical nanocage and is therefore accessible for the genetic fusion of proteins of interest. Upon

108 folding, apoferritin protomers act as building blocks that drive the multimerization of the 24
109 proteins fused to their N termini (**Fig. 1a**).

110 First, we investigated the impact of multivalency on the ability of the single chain variable domain
111 VHH-72 to block viral infection. VHH-72 has been previously described to neutralize SARS-CoV-
112 2 when fused to a Fc domain, but not in its monovalent format³⁰. The light chain of human
113 apoferritin displaying 24 copies of VHH-72 assembled into monodisperse, well-formed spherical
114 particles (**Fig. 1b-c**) and showed an enhanced binding avidity to the S protein (**Fig. 1d**) in
115 comparison to bivalent VHH-72-Fc. Strikingly, display of VHH-72 on the light chain of human
116 apoferritin achieved a 1000-fold increase in neutralization potency against SARS-CoV-2
117 pseudovirus (PsV) compared to the conventional Fc fusion (**Fig. 1e**).

118

119 **Multabodies have IgG-like properties**

120 The Fc confers *in vivo* half-life and effector functions to IgGs through interaction with neonatal
121 Fc receptor (FcRn) and Fc gamma receptors (Fc γ R), respectively. To confer these IgG-like
122 properties to the MB, we next sought to incorporate both Fabs and Fc domains. Because a Fab is
123 a hetero-dimer consisting of a light and a heavy chain, and the Fc is a homodimer, we created
124 single-chain Fab (scFab) and Fc (scFc) polypeptide constructs to allow for their direct fusion to
125 the N terminus of the apoferritin protomer. As a first step, we generated a species-matched
126 surrogate molecule that consists of mouse light chain apoferritin fusions to a mouse scFab and a
127 mouse scFc (IgG2a subtype), or a modified mouse scFc (LALAP mutation) to assess their,
128 biodistribution, immunogenicity and pharmacokinetics *in vivo* (**Fig. S1**). As expected, binding
129 affinity of the WT MB to mouse Fc receptors was enhanced in comparison to the parental IgG and

130 the LALAP mutation reduced binding affinity to Fc γ R1 (**Fig. S1a**) Subcutaneous administration
131 of these MBs in C57BL/6 or BALB/c mice was well tolerated with no decrease in body weight or
132 visible adverse events. *In vivo* bioavailability and biodistribution of the MB were similar to the
133 parental IgG (**Fig. S1b and c**). Confirming the role of the Fc in mediating *in vivo* bioavailability,
134 serum half-life could be extended by mutations in the Fc (**Fig. S1b**). Presumably because all
135 sequences derived from the host, the MB did not induce an anti-drug antibody response in mice
136 (**Fig. S1d**).

137 In view of these results, we aimed to generate MBs derived from the previously reported IgG
138 BD23⁵ and 4A8⁶ that target the SARS-CoV-2 spike RBD and N-terminal domain (NTD),
139 respectively. Addition of scFc's into the MB reduces the number of scFabs that can be
140 multimerized. In order to endow the MB platform with Fc without compromising Fab avidity and
141 hence neutralization potency, we engineered the apoferritin protomer to accommodate more than
142 24 components per particle. Based on its four-helical bundle fold, the human apoferritin protomer
143 was split into two halves: the two N-terminal α helices (N-Ferritin) and the two C-terminal α
144 helices (C-Ferritin). In this configuration, the scFc fragment of human IgG1 and the scFab of anti-
145 SARS-CoV-2 IgGs were genetically fused at the N terminus of each apoferritin half, respectively.
146 Split apoferritin complementation led to hetero-dimerization of the two halves and in turn, full
147 apoferritin self-assembly displaying more than 24 copies of scFc and scFab on the nanocage
148 periphery (**Fig. 2a**). Conveniently, this design allows for the straightforward purification of the
149 MB using Protein A akin to IgG purification.

150 This split MB design forms 16 nm hydrodynamic radius (R_h) spherical particles with an
151 uninterrupted ring of density and regularly spaced protruding scFabs and scFc (**Fig. 2b and 2c**).
152 Hence, the MB is on the lower size range of natural IgMs³³ but packs more weight on a similar

153 size to achieve multi-valency and multi-specificity. Binding kinetics experiments demonstrated
154 that avidity of the MB for the Spike was preserved upon addition of Fc fragments (**Fig. 2d**).
155 Binding to human Fc γ RI and FcRn at endosomal pH confirmed that scFc was properly folded in
156 the split MB design and that LALAP and I253A mutations lowered binding affinities to Fc γ RI and
157 FcRn, respectively (**Fig. 2e**). SARS-CoV-2 PsV neutralization assays with the split design MBs
158 showed that enhanced binding affinity for the S protein translates into an improved neutralization
159 potency in comparison to their IgG counterparts, with a ~1600-fold and ~2500-fold increase for
160 BD23 and A48, respectively (**Fig. 2f**). Combined, this data supported the further exploration of
161 the MB as an IgG-like platform that confers extraordinary multivalency.

162

163 **From antibody discovery to ultrapotent neutralizers**

164 We next assessed the ability of the MB platform to transform mAb binders identified from initial
165 phage display screens into potent neutralizers against SARS-CoV-2 (**Fig. 3a**). Following standard
166 biopanning protocols, 20 human mAb binders with moderate affinities that range from 10^{-6} to 10^{-
167 8 M against the RBD of SARS-CoV-2 were selected (**Table S1**). These mAbs were produced as
168 full-length IgGs and MBs and their capacity to block viral infection was compared in a
169 neutralization assay against SARS-CoV-2 PsV (**Fig. 3b** and **Fig. S2a**). Notably, MBs preserved
170 the thermostability of their parental IgGs (**Fig. S2b-c**) and significantly enhanced the potency of
171 18 out of 20 (90%) IgGs by up to four orders of magnitude. The largest increment was observed
172 for mAb 298 which went from an IC₅₀ of ~30 μ g/mL as an IgG to 0.0001 μ g/mL as a MB.
173 Strikingly, 11 mAbs were converted from non-neutralizing IgGs to neutralizing MBs in the tested
174 concentration ranges. Seven MBs displayed exceptional potency with IC₅₀ values between 0.2-2
175 ng/mL against SARS-CoV-2 PsV using two different target cells (293T-ACE2 and HeLa-ACE2

176 cells) (**Fig. 3b** and **Fig. S3a**). The enhanced neutralization potency of the MB was further
177 confirmed with authentic SARS-CoV-2 virus for the mAbs with the highest potency (**Fig. 3c** and
178 **Fig. S3b**). Retrospectively, all IgGs and MBs were tested for their ability to bind to the S protein
179 and the RBD of SARS-CoV-2 (**Fig. S4**). Increased avidity resulted in higher apparent binding
180 affinities with no detectable off-rates against the S protein, most likely due to inter-spike
181 crosslinking that translates into high neutralization potency (**Fig. 3b-d** and **Fig. S4**). Overall, the
182 data shows that the MB platform is compatible with rapid delivery of ultrapotent IgG-like
183 molecules.

184

185 **Epitope mapping**

186 Based on their neutralization potency, seven mAbs were selected for further characterization: 298
187 (IGHV1-46/IGKV4-1), 82 (IGHV1-46/IGKV1-39), 46 (IGHV3-23/IGKV1-39), 324 (IGHV1-
188 69/IGKV1-39), 236 (IGHV1-69/IGKV2-28), 52 (IGHV1-69/IGKV1-39) and 80 (IGHV1-
189 69/IGKV4-1) (**Fig. 3b** and **Table S1**). Epitope binning experiments showed that these mAbs target
190 two main sites on the RBD, with one of these bins overlapping with the ACE2 binding site (**Fig.**
191 **4a** and **Fig. S5**). Cryo-EM structures of Fab-SARS-CoV-2 S complexes at a global resolution of
192 ~6-7 Å confirmed that mAbs 324, 298, 80 bind overlapping epitopes (**Fig. 4b**, **Fig. S6a-c** and
193 **Table S2**). To gain insight into the binding of mAbs targeting the second bin, we obtained the
194 cryo-EM structure of Fab 46 in complex with the RBD at a global resolution of 4.0 Å (**Fig. 4c**,
195 **Fig. S6d** and **Table S2**), and the crystal structure of Fabs 298 and 52 as a ternary complex with
196 the RBD at 2.95 Å resolution (**Fig. 4d**, **Fig. S7** and **Table S3**).
197 The crystal structure shows that mAb 298 binds almost exclusively to the ACE2 receptor binding
198 motif (RBM) of the RBD (residues 438-506). In fact, out of 16 RBD residues involved in binding

199 mAb 298, 12 are also involved in ACE2-RBD binding (**Fig. S7a-c** and **Table S4 and S5**). The
200 RBM is stabilized by 11 hydrogen bonds from heavy and light chain residues of mAb 298. In
201 addition, RBM Phe486 is contacted by 11 mAb 298 residues burying approximately 170 Å² (24%
202 of the total buried surface area on RBD) and hence is central to the antibody-antigen interaction
203 (**Fig. S7a** and **Table S5**).

204 Detailed analysis of the RBD-52 Fab interface reveals that the epitope of mAb 52 is shifted towards
205 the core of the RBD encompassing 20 residues of the RBM and 7 residues in the core domain (**Fig.**
206 **4c**, **Fig. S7b** and **Table S6 and S7**). In agreement with the competition data, antibody 52 and
207 antibody 46 share a similar binding site, although they approach the RBD with slightly different
208 angles (**Fig. 4c-d** and **Fig. S7d**). Inspection of previously reported structures of RBD-antibody
209 complexes reveal that antibodies 46 and 52 target a site of vulnerability on the SARS-CoV-2 spike
210 that has not been described previously (**Fig. 4e**). The epitope targeted by these antibodies is
211 partially occluded by the NTD in the S “closed” conformation, suggesting that the mechanism of
212 action for this new class of antibodies could involve Spike destabilization. Together, these data
213 demonstrate that the enhanced potency observed for the MB platform is associated with mAbs that
214 target both overlapping and distinct epitope bins.

215

216 **Multabodies overcome Spike sequence variability**

217 To explore whether MBs could resist viral escape, we tested the effect of four naturally occurring
218 RBD mutations (L452R, A475V, N439K and V483A)³⁴ (**Fig. 5a**) on the binding and neutralization
219 of the seven human mAbs of highest potency (**Fig. 5b-c**). In addition, the impact of mutating
220 Asn234, a glycosylation site, to Gln was also assessed because the absence of glycosylation at this

site has been previously reported to decrease sensitivity to neutralizing antibodies targeting the RBD³⁴. The more infectious PsV variant D614G³⁵ was also included in the panel. Mutation L452R significantly decreased binding and potency of antibodies 52 and 46, while antibody 298 was sensitive to mutation A475V (**Fig. 5b-c**). Deletion of the N-linked glycan at position Asn234 increased viral resistance to the majority of the antibodies, especially mAbs 46, 80 and 324, emphasizing the important role of glycans in viral antigenicity (**Fig. 5c**). Strikingly, the following mAbs were minimally impacted in their exceptional neutralization potency by any S mutation when present in the MB format: 298, 80, 324, and 236 (**Fig. 5d**). Mutation L452R decreased the sensitivity of the 46-MB and 52-MB but in contrast to their parental IgGs, they remained neutralizing against this PsV variant (**Fig. 5d**). The more infectious SARS-CoV-2 PsV variant D614G was neutralized with similar potency as the WT PsV for both IgGs and MBs (**Fig. 5c** and **Fig. S8a**).

MB cocktails consisting of three monospecific MB resulted in pan-neutralization across all PsV variants without a significant loss in potency and hence achieved a 100-1000-fold higher potency compared to the corresponding IgG cocktails (**Fig. 5e** and **Fig. S8c-d**). In order to achieve breadth within a single molecule, we next generated tri-specific MBs by combining multimerization subunits displaying three different Fabs in the same MB assembly (**Fig. S8b**). Notably, the resulting tri-specific MBs exhibited pan-neutralization while preserving the exceptional neutralization potency of the monospecific versions (**Fig. 5e** and **Fig. S8c-d**). The most notable increase in potency was for the 298-324-46 combination, where the IgG cocktail neutralized WT SARS-CoV-2 PsV with an ~0.5 µg/mL (3.3×10^{-9} M) IC₅₀, while the tri-specific MB achieved broad neutralization with an exceptional IC₅₀ of ~0.0005 µg/mL (2.2×10^{-13} M). The potency

243 enhancement of MB cocktails and tri-specific MBs in comparison to their corresponding IgG tri-
244 specific cocktails was also observed with live replicating SARS-CoV-2 virus (**Fig. S8e**).

245

246 Discussion

247 We have developed an antibody-multimerization platform to increase avidity of mAbs targeting
248 SARS-CoV-2. The seven most potent MBs have IC₅₀ values of 0.2 to 2 ng/mL (9 × 10⁻¹⁴ to 9 × 10⁻
249 ¹³ M) against SARS-CoV-2 PsVs and therefore are, to our knowledge, within the most potent
250 antibody-like molecules reported to date against SARS-CoV-2.

251 The MB platform was designed to include key favorable attributes from a developability
252 perspective. First, the ability to augment antibody potency is independent of antibody sequence,
253 format or epitope targeted. The modularity and flexibility of the platform was exemplified by
254 enhancing the potency of a VHH and multiple Fabs that target non-overlapping regions on two
255 SARS-CoV-2 S sub-domains (RBD and NTD). Second, in contrast to other approaches to enhance
256 avidity such as tandem fusions of single chain variable fragments^{36,37}, which suffer from low
257 stability, MBs self-assemble into highly stable particles with aggregation temperatures values
258 similar to those of their parental IgGs. Third, alternative multimerization strategies like
259 streptavidin³⁸, verotoxin B subunit scaffolds³⁹ or viral-like nanoparticles⁴⁰ face immunogenicity
260 challenges and/or poor bioavailability because of the absence of an Fc fragment and therefore the
261 inability to undergo FcRn-mediated recycling. The light chain of apoferritin is fully human,
262 biologically inactive, has been engineered to include Fc domains, and despite multimerization of
263 >24 Fab/Fc fragments, has a hydrodynamic radius similar to an IgM. As such, a surrogate mouse
264 MB did not elicit anti-drug antibodies in mice, was detectable in the sera for over a week, and has
265 similar biodistribution as its parental IgG.

266 Different increases in neutralization potency were observed for different mAb sequences tested on
267 the MB against SARS-CoV-2. This suggests that the ability of the MB to enhance potency may
268 depend on epitope location on the Spike or the geometry of how the Fabs engage the antigen to
269 achieve neutralization. The fact that 2 out of 20 SARS-CoV-2 RBD binders were not rescued by
270 the MB platform also suggests limitations based on mAb sequences and binding properties.
271 Nevertheless, the capacity of the MB to transform avidity into neutralization potency across a
272 range of epitope specificities on the SARS-CoV-2 Spike highlights the potential for using this
273 technology broadly. It will be interesting to explore the potency-enhancement capacity of the MB
274 platform against viruses with low surface spike density like HIV⁴¹, or against other targets like the
275 tumor necrosis factor receptor superfamily, where bivalency of conventional antibodies limits their
276 efficient activation⁴².

277 Virus escape can arise in response to selective pressure from treatments or during natural selection.
278 A conventional approach to combat escape mutants is the use of antibody cocktails targeting
279 different epitopes. MBs showed a lower susceptibility to S mutations in comparison to their
280 parental IgGs, presumably because the loss in affinity was compensated by enhanced binding
281 avidity. Hence, when used in cocktails, the MB overcame viral sequence variability with
282 exceptional potency. In addition, the split MB design allows combination of multiple antibody
283 specificities within a single multimerized molecule resulting in similar potency and breadth as the
284 MB cocktails. To our knowledge, these MBs represent the first tri-specifics described against
285 SARS-CoV-2. Multi-specificity within the same particle could offer additional advantages such as
286 intra-S avidity and synergy for the right combination of mAbs, setting the stage for further
287 investigation of different combinations of mAb specificities on the MB.

288 Overall, the MB platform provides a tool to surpass antibody affinity limits and generate broad
289 and potent neutralizing molecules without the need for extensive antibody discovery or
290 engineering efforts. This platform will accelerate the timeline from discovery to development of
291 antibodies as medical countermeasures against COVID-19 and in future pandemics.

292

293 **References**

- 294 1. Connor, E. M. Palivizumab, a humanized respiratory syncytial virus monoclonal antibody,
295 reduces hospitalization from respiratory syncytial virus infection in high-risk infants.
296 *Pediatrics* **102**, 531–537 (1998).
- 297 2. Mulangu, S. *et al.* A randomized, controlled trial of Ebola virus disease therapeutics. *N.
298 Engl. J. Med.* **381**, 2293–2303 (2019).
- 299 3. Ju, B. *et al.* Human neutralizing antibodies elicited by SARS-CoV-2 infection. *Nature*
300 **584**, 115–119 (2020).
- 301 4. Liu, L. *et al.* Potent neutralizing antibodies against multiple epitopes on SARS-CoV-2
302 spike. *Nature* **584**, 450–456 (2020).
- 303 5. Cao, Y. *et al.* Potent Neutralizing Antibodies against SARS-CoV-2 Identified by High-
304 Throughput Single-Cell Sequencing of Convalescent Patients' B Cells. *Cell* **182**, 73–84
305 (2020).
- 306 6. Chi, X. *et al.* A neutralizing human antibody binds to the N-terminal domain of the Spike
307 protein of SARS-CoV-2. *Science* **369**, 650–655 (2020).
- 308 7. Seydoux, E. *et al.* Analysis of a SARS-CoV-2-Infected Individual Reveals Development
309 of Potent Neutralizing Antibodies with Limited Somatic Mutation. *Immunity* **53**, 98–105
310 (2020).

- 311 8. Pinto, D. *et al.* Cross-neutralization of SARS-CoV-2 by a human monoclonal SARS-CoV
312 antibody. *Nature* (2020).
- 313 9. Barnes, C. O. *et al.* Structures of Human Antibodies Bound to SARS-CoV-2 Spike Reveal
314 Common Epitopes and Recurrent Features of Antibodies. *Cell* (2020).
- 315 10. Shi, R. *et al.* A human neutralizing antibody targets the receptor-binding site of SARS-
316 CoV-2. *Nature* (2020).
- 317 11. Rogers, T. F. *et al.* Isolation of potent SARS-CoV-2 neutralizing antibodies and protection
318 from disease in a small animal model. *Science*. **369**, 956–963 (2020).
- 319 12. Brouwer, P. J. M. *et al.* Potent neutralizing antibodies from COVID-19 patients define
320 multiple targets of vulnerability. *Science* **369**, 643–650 (2020).
- 321 13. Wang, C. *et al.* A human monoclonal antibody blocking SARS-CoV-2 infection. *Nat.
322 Commun.* **11**, (2020).
- 323 14. Zost, S. J. *et al.* Potently neutralizing and protective human antibodies against SARS-
324 CoV-2. *Nature* **584**, 443–449 (2020).
- 325 15. Baum, A. *et al.* Antibody cocktail to SARS-CoV-2 spike protein prevents rapid mutational
326 escape seen with individual antibodies. *Science*. **369**, 1014–1018 (2020).
- 327 16. Hansen, J. *et al.* Studies in humanized mice and convalescent humans yield a SARS-CoV-
328 2 antibody cocktail. *Science*. **369**, 1010–1014 (2020).
- 329 17. Lv, Z. *et al.* Structural basis for neutralization of SARS-CoV-2 and SARS-CoV by a
330 potent therapeutic antibody. *Science*. **369**, 1505–1509 (2020).
- 331 18. Tortorici, M. A. *et al.* Ultrapotent human antibodies protect against SARS-CoV-2
332 challenge via multiple mechanisms. *Science*. (2020).
- 333 19. Zhou, D. *et al.* Structural basis for the neutralization of SARS-CoV-2 by an antibody from

- 334 a convalescent patient. *Nat. Struct. Mol. Biol.* (2020).
- 335 20. Study Assessing the Efficacy and Safety of Anti-Spike SARS CoV-2 Monoclonal
336 Antibodies for Prevention of SARS CoV-2 Infection Asymptomatic in Healthy Adults
337 Who Are Household Contacts to an Individual With a Positive SARS-CoV-2 RT-PCR
338 Assay - Full Text Vi.
- 339 21. A Study of LY3819253 (LY-CoV555) and LY3832479 (LY-CoV016) in Participants
340 With Mild to Moderate COVID-19 Illness - Full Text View - ClinicalTrials.gov.
- 341 22. Hoffmann, M. *et al.* SARS-CoV-2 Cell Entry Depends on ACE2 and TMPRSS2 and Is
342 Blocked by a Clinically Proven Protease Inhibitor. *Cell* **181**, 271–280 (2020).
- 343 23. van Dorp, L. *et al.* Emergence of genomic diversity and recurrent mutations in SARS-
344 CoV-2. *Infect. Genet. Evol.* **83**, (2020).
- 345 24. Sok, D. & Burton, D. R. Recent progress in broadly neutralizing antibodies to HIV. *Nat.*
346 *Immunol.* **11**, 1179–1188 (2018).
- 347 25. Laursen, N. S. & Wilson, I. A. Broadly neutralizing antibodies against influenza viruses.
348 *Antiviral Res.* **98**, 476–483 (2013).
- 349 26. Bornholdt, Z. A. *et al.* Isolation of potent neutralizing antibodies from a survivor of the
350 2014 Ebola virus outbreak. *Science*. **351**, 1078–1083 (2016).
- 351 27. Wu, H. *et al.* Ultra-potent antibodies against respiratory syncytial virus: Effects of binding
352 kinetics and binding valence on viral neutralization. *J. Mol. Biol.* **350**, 126–144 (2005).
- 353 28. Icenogle, J. *et al.* Neutralization of poliovirus by a monoclonal antibody: Kinetics and
354 stoichiometry. *Virology* **127**, 412–425 (1983).
- 355 29. Cavacini, L. A., Emes, C. L., Power, J., Duval, M. & Posner, M. R. Effect of antibody
356 valency on interaction with cell-surface expressed HIV- 1 and viral neutralization. *J.*

- 357 *Immunol.* **152**, 2538–2545 (1994).
- 358 30. Wrapp, D. *et al.* Structural Basis for Potent Neutralization of Betacoronaviruses by
359 Single-Domain Camelid Antibodies. *Cell* (2020).
- 360 31. Li, W. *et al.* High potency of a bivalent human VH domain in SARS-CoV-2 animal
361 models. *Cell* **183**, 1–13 (2020).
- 362 32. Lawson, D. M. *et al.* Solving the structure of human H ferritin by genetically engineering
363 intermolecular crystal contacts. *Nature* **349**, 541–544 (1991).
- 364 33. Radomsky, M. L., Whaley, K. J., Cone, R. A. & Saltzman, W. M. Macromolecules
365 released from polymers: diffusion into unstirred fluids. *Biomaterials* **11**, 619–624 (1990).
- 366 34. Li, Q. *et al.* The Impact of Mutations in SARS-CoV-2 Spike on Viral Infectivity and
367 Antigenicity. *Cell* **182**, 1284–1294 (2020).
- 368 35. Korber, B. *et al.* Tracking Changes in SARS-CoV-2 Spike: Evidence that D614G
369 Increases Infectivity of the COVID-19 Virus. *Cell* **182**, 812–827 (2020).
- 370 36. Miller, K. *et al.* Design, Construction, and In Vitro Analyses of Multivalent Antibodies. *J.*
371 *Immunol.* **170**, 4854–4861 (2003).
- 372 37. Kipriyanov, S. M. *et al.* Bispecific tandem diabody for tumor therapy with improved
373 antigen binding and pharmacokinetics. *J. Mol. Biol.* **293**, 41–56 (1999).
- 374 38. Kipriyanov, S. M. *et al.* Affinity enhancement of a recombinant antibody: Formation of
375 complexes with multiple valency by a single-chain Fv fragment-core streptavidin fusion.
376 *Protein Eng.* **9**, 203–211 (1996).
- 377 39. Zhang, J. *et al.* Pentamerization of single-domain antibodies from phage libraries: A novel
378 strategy for the rapid generation of high-avidity antibody reagents. *J. Mol. Biol.* **335**, 49–
379 56 (2004).

- 380 40. Hoffmann, M. A. G. *et al.* Nanoparticles presenting clusters of CD4 expose a universal
381 vulnerability of HIV-1 by mimicking target cells. *Proc. Natl. Acad. Sci. U. S. A.* **117**,
382 18719–18728 (2020).
- 383 41. Zhu, P. *et al.* Electron tomography analysis of envelope glycoprotein trimers on HIV and
384 simian immunodeficiency virus virions. *Proc. Natl. Acad. Sci. U. S. A.* **100**, 15812–15817
385 (2003).
- 386 42. Wajant, H. Principles of antibody-mediated TNF receptor activation. *Cell Death Differ.*
387 **22**, 1727–1741 (2015).
- 388 43. Schlothauer, T. *et al.* Novel human IgG1 and IgG4 Fc-engineered antibodies with
389 completely abolished immune effector functions. *Protein Eng. Des. Sel.* **29**, 457–466
390 (2016).
- 391 44. Crawford, K. H. D. *et al.* Protocol and reagents for pseudotyping lentiviral particles with
392 SARS-CoV-2 spike protein for neutralization assays. *Viruses* **12**, 513 (2020).
- 393 45. Banerjee, A. *et al.* Isolation, Sequence, Infectivity, and Replication Kinetics of Severe
394 Acute Respiratory Syndrome Coronavirus 2. *Emerg. Infect. Dis.* **26**, (2020).
- 395 46. Lan, J. *et al.* Structure of the SARS-CoV-2 spike receptor-binding domain bound to the
396 ACE2 receptor. *Nature* **581**, 215–220 (2020).
- 397 47. Yuan, M. *et al.* A highly conserved cryptic epitope in the receptor binding domains of
398 SARS-CoV-2 and SARS-CoV. *Science*. **368**, 630–633 (2020).
- 399 48. Hurlburt, N. K. *et al.* Structural basis for potent neutralization of SARS-CoV-2 and role of
400 antibody affinity maturation. *bioRxiv* (2020).
- 401
- 402

403 **Acknowledgements**

404 We thank F Krammer for providing the WT SARS-CoV-2 Spike plasmid. We thank JD Bloom
405 and AC Gingras for access to 293T-ACE2 cells and reagents to make the SARS-CoV-2 PsV. We
406 thank DR Burton for providing HeLa-ACE2 cells and the SARS-CoV-2 Spike mutant D614G. We
407 are thankful to C Pettus, J Wang, D Pineda and K Patel for their work panning the SuperHuman
408 2.0 library against the SARS-CoV-2 RBD and characterizing binders. We thank JM Jorgensen and
409 S Popa for assistance with the Octet RED96 and Unit Instruments. The following reagents were
410 produced under HHSN272201400008C and obtained through BEI Resources, NIAID, NIH:
411 Vector pCAGGS Containing the SARS-Related Coronavirus 2, Wuhan-Hu-1 Spike Glycoprotein
412 Receptor Binding Domain (RBD), NR-52309, Vector pCAGGS Containing the SARS-Related
413 Coronavirus 2, Wuhan-Hu-1 Spike Glycoprotein Gene (soluble, stabilized), NR-52394. **Funding:**
414 This work was supported by Natural Sciences and Engineering Research Council of Canada
415 discovery grant 6280100058 (JPJ), by operating grant PJ4-169662 from the Canadian Institutes of
416 Health Research (CIHR; BT, JPJ), by COVID-19 Research Fund C-094-2424972-JULIEN (JPJ)
417 from the Province of Ontario Ministry of Colleges and Universities, and by the Hospital for Sick
418 Children Foundation. This research was also supported by the European Union's Horizon 2020
419 research and innovation program under Marie Skłodowska-Curie grant 790012 (ER), by a Hospital
420 for Sick Children Restracom Postdoctoral Fellowship (IK), by a CIHR Postdoctoral Fellowship
421 (YZT), by a NSERC postgraduate doctoral scholarship (TZ), by a Vanier Canada Graduate
422 Scholarship (TS), by a CIHR Canada Graduate Scholarship - Master's Award (AN), by the CIFAR
423 Azrieli Global Scholar program (JPJ), by the Ontario Early Researcher Awards program (JPJ), and
424 by the Canada Research Chairs program (JLR, BT, JPJ). Cryo-EM data was collected at the
425 Toronto High Resolution High Throughput cryo-EM facility, biophysical data at the Structural &

426 Biophysical Core facility, and biodistribution data at the CFI 3D Facility at University of Toronto,
427 all supported by the Canada Foundation for Innovation and Ontario Research Fund. X-ray
428 diffraction experiments were performed at GM/CA@APS, which has been funded in whole or in
429 part with federal funds from the National Cancer Institute (ACB-12002) and the National Institute
430 of General Medical Sciences (AGM-12006). The Eiger 16M detector at GM/CA-XSD was funded
431 by NIH grant S10 OD012289. This research used resources of the Advanced Photon Source, a
432 U.S. Department of Energy (DOE) Office of Science user facility operated for the DOE Office of
433 Science by Argonne National Laboratory under contract DE-AC02-06CH11357. **Author**
434 **contributions:** ER, BT and JPJ conceived the research and designed the experiments; ER, IK,
435 YZT, SB, HC, TZ, GW, PB, FG, JN, TS, AS, KM, AN, KP, SB, SY and SLC performed
436 experimental work. JG, NCH, SM and SDGO provided critical reagents and expertise. ER, IK,
437 YCT, BT, JLR and JPJ analyzed the data. ER and JPJ wrote the manuscript with input from all
438 authors. **Competing interests:** The Hospital for Sick Children has applied for patents concerning
439 SARS-CoV-2 antibodies and the Multobody platform technology that are related to this work. BT
440 and JPJ are founders of Radiant Biotherapeutics and are members of its Scientific Advisory Board.
441 SY, SLC and JG are employees of DistributedBio and may hold shares in DistributedBio. All other
442 authors declare no competing interests. **Data and materials availability:** The electron microscopy
443 maps have been deposited at the Electron Microscopy Data Bank (EMDB) with accession codes
444 EMD-22738, EMD-22739, EMD-22740, EMD-22741 (Table S2). The crystal structure of 298-52-
445 RBD complex (Table S3) is available from the Protein Data Bank under accession code PDB:
446 7K9Z. Sequences of the monoclonal antibodies are available in Table S1. Other data are available
447 from the corresponding author upon reasonable request.

448

449 **SUPPLEMENTARY MATERIALS**

450 Materials and Methods

451 Figs S1 to S8

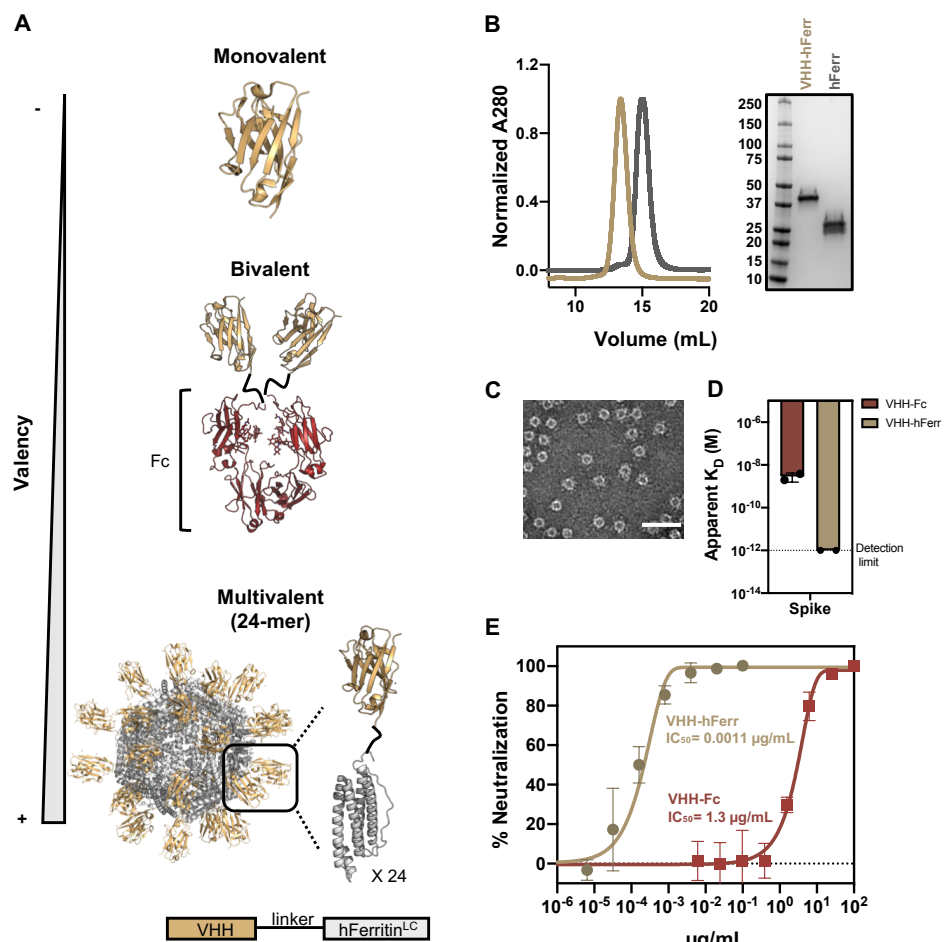
452 Tables S1 to S7

453 References (46-49)

454

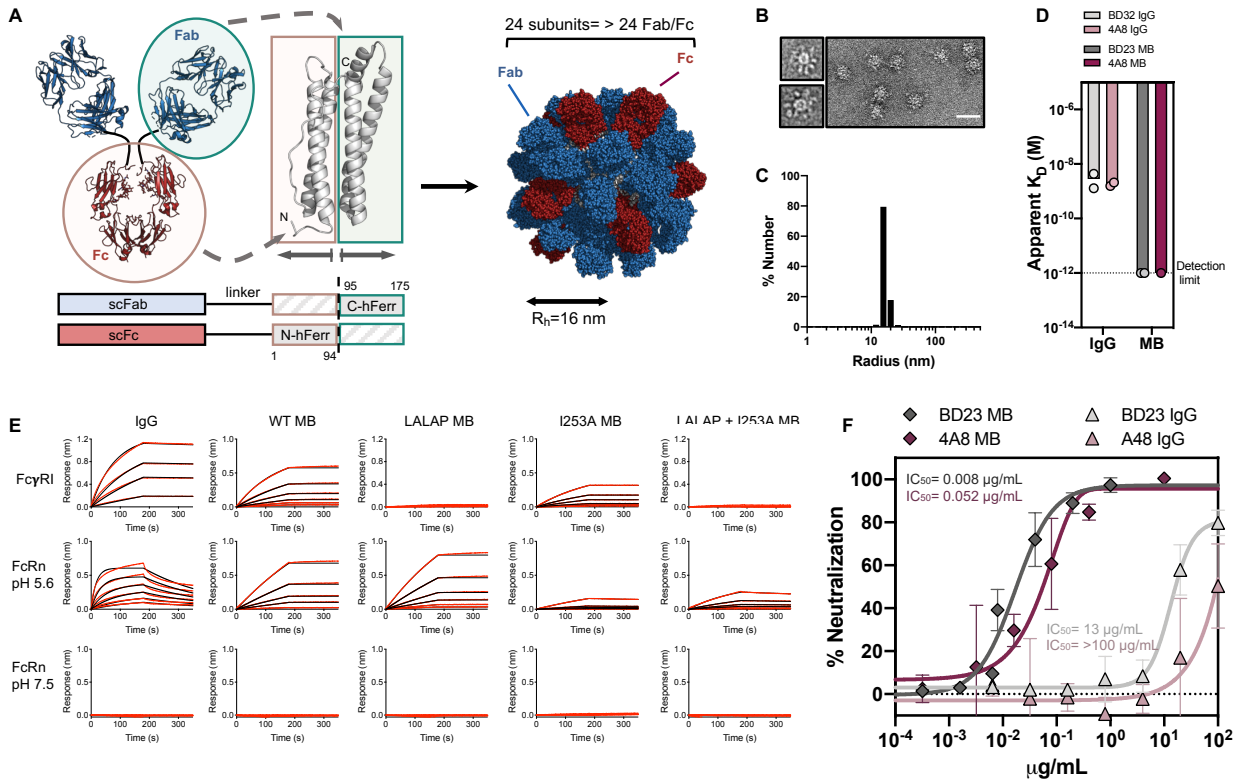
455

456 **Figures**



457

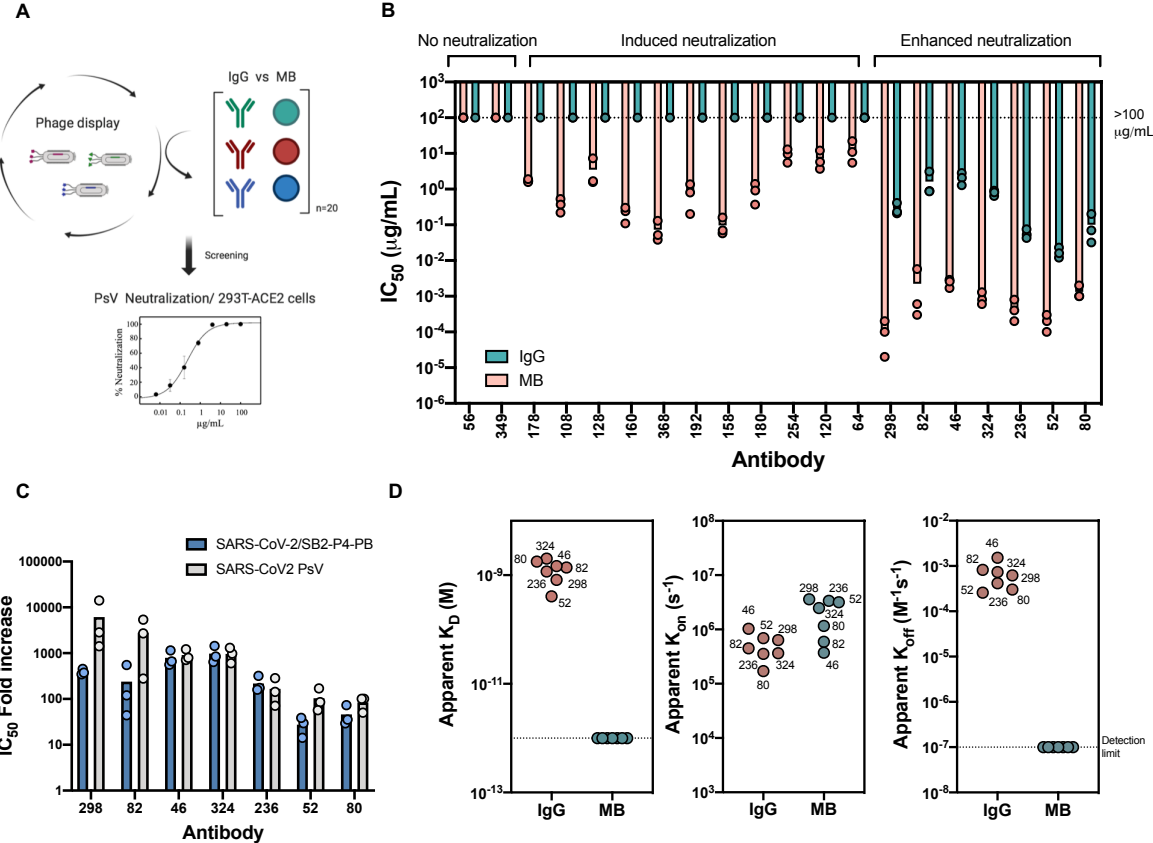
458 **Fig. 1. Avidity enhances binding and neutralization of VHH against SARS-CoV-2. (A)**
459 Schematic representation of a monomeric VHH domain and its multimerization using a
460 conventional Fc scaffold or human apoferritin. **(B)** Size exclusion chromatography and SDS-
461 PAGE of apoferritin alone (gray) and VHH-72 apoferritin particles (gold). **(C)** Negative stain
462 electron microscopy of VHH-72 apoferritin particles. (Scale bar 50 nm). **(D)** Comparison of the
463 binding avidity (apparent K_D) of VHH-72 to SARS-CoV-2 S protein when displayed in a bivalent
464 (red) or 24-mer (gold) format. Apparent K_D higher than 10^{-12} M (dash line) is beyond the
465 instrument detection limit. **(E)** Neutralization potency against SARS-CoV-2 PsV (color coding is
466 as in d). One representative out of two experiments with similar results is shown.



467

468 **Fig. 2. Protein engineering to multimerize IgG-like particles against SARS-CoV-2. (A)**
469 Schematic representation of the human apo ferritin split design. **(B)** Negative stain electron
470 micrograph of the MB. (Scale bar 50 nm). **(C)** Hydrodynamic radius (R_h) of the MB. **(D)** Avidity
471 effect on the binding (apparent K_D) of A48 (purple) and BD23 (gray) to the SARS-CoV-2 Spike.
472 **(E)** Kinetic curves of BD23 IgG and MB with different Fc sequence variants binding to Fc γ RI (top
473 row), FcRn at endosomal pH (middle row) and FcRn at physiological pH (bottom row). Black
474 lines represent raw data whereas red lines represent global fits. **(F)** Neutralization of SARS-CoV-
475 2 PsV by A48 and BD23 IgGs and MBs. The mean values \pm SD for two technical replicates for a
476 representative experiment is shown.

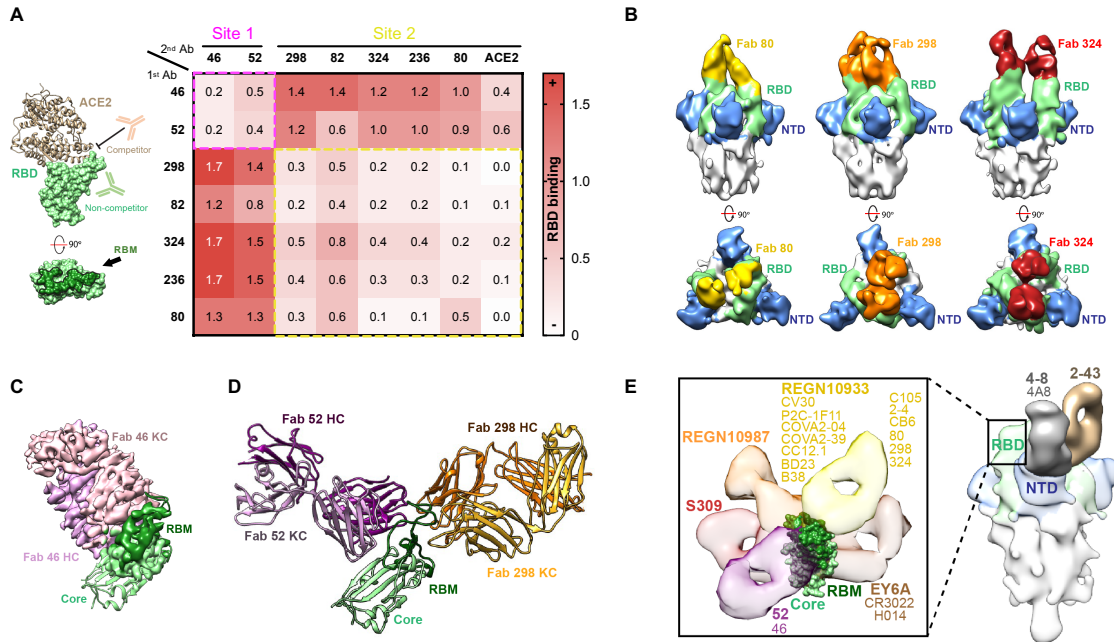
477



478

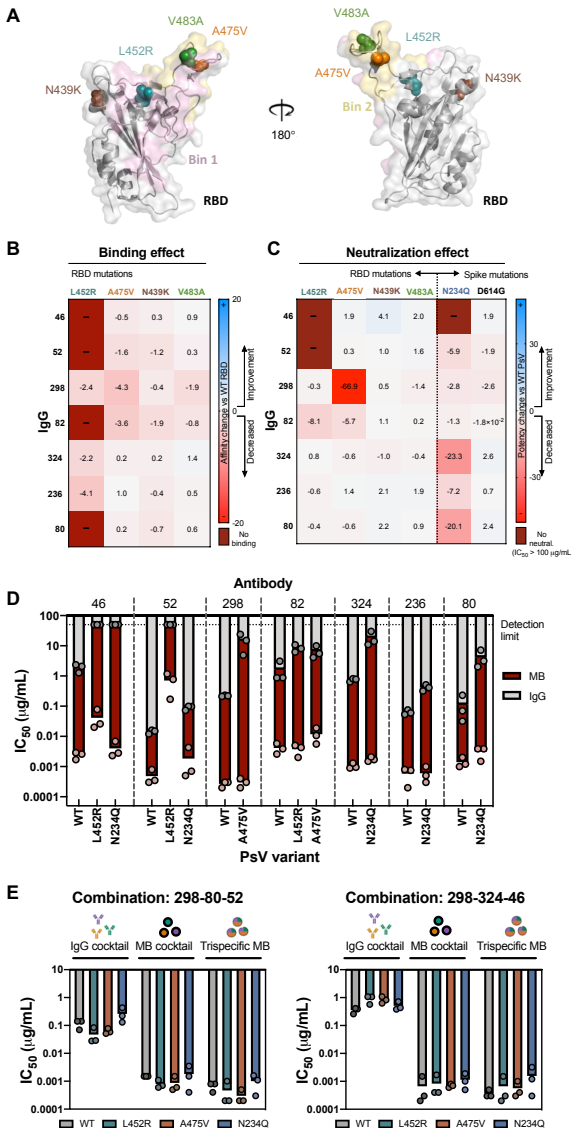
479 **Fig. 3. The Multabody enhances the potency of human mAbs from phage display. (A)** Work
 480 flow for the identification of potent anti-SARS-CoV-2 neutralizers using the MB technology. **(B)**
 481 Comparison of neutralization potency between IgGs and MBs that display the same human Fab
 482 sequences derived from phage display. **(C)** IC₅₀ values fold increase upon multimerization. **(D)**
 483 Apparent affinity (K_D), association (k_{on}) and dissociation (k_{off}) rates of the most potent neutralizing
 484 MBs compared to their IgG counterparts for binding the SARS-CoV-2 S protein. Three biological
 485 replicates and their mean are shown for IC₅₀ values in (b) and (c).

486



487

488 **Fig. 4. Epitope delineation of the most potent mAb specificities.** (A) Surface and cartoon
 489 representation of RBD (*light green* for the core and *dark green* for RBM) and ACE2⁴⁶ (*light*
 490 *brown*) binding. Heat map showing binding competition experiments. Epitope bins are highlighted
 491 by dashed-line boxes. (B) 15.0 Å filtered cryo-EM reconstruction of the Spike (*grey*) in complex
 492 with Fab 80 (*yellow*), 298 (*orange*) and 324 (*red*). The RBD and NTD are shown in *green* and
 493 *blue*, respectively. (C) Cryo-EM reconstruction of Fab 46 (*pink*) and RBD (*green*) complex. A
 494 RBD cartoon⁴⁶ is fitted into the partial density observed for the RBD. (D) Crystal structure of the
 495 ternary complex formed by Fab 52 (*purple*), Fab 298 (*orange*) and RBD (*green*). (E) Composite
 496 image depicting antibodies targeting SARS-CoV-2 S with available PDB or EMD
 497 entries^{3,4,6,8,10,16,17,47,48}. Inset: close up view of antibodies targeting different antigenic sites on the
 498 RBD. The mAb with the lowest reported IC₅₀ value against SARS-CoV-2 PsV was selected as a
 499 representative antibody of the bin (color coding as in b).



500

501 **Fig. 5. Multabodies overcome SARS-CoV-2 sequence diversity.** (A) Cartoon representation of
502 the RBD showing four naturally occurring mutations as spheres. The epitopes of mAbs 52 (*light*
503 *pink*) and 298 (*yellow*) are shown as representative epitopes of each bin. (B) Affinity and (C) IC₅₀
504 fold-change comparison between WT and mutated RBD and PsV, respectively. (D) Neutralization
505 potency of IgG (*grey bars*) vs MB (*dark red bars*) against SARS-CoV-2 PsV variants in
506 comparison to WT PsV. (E) Neutralization potency comparison of two IgG cocktails (three IgGs),
507 monospecific MB cocktails (three MBs) and tri-specific MBs against WT SARS-CoV-2 PsV and

508 variants. mAbs sensitive to one or more PsV variants were selected to generate the cocktails and
509 the tri-specific MBs. The mean of three biological replicates are shown in (b), (c), (d) and (e).

510

Supplementary Materials for

Multivalency transforms SARS-CoV-2 antibodies into broad and ultrapotent neutralizers

Edurne Rujas^{1,2,3}, Iga Kucharska¹, Yong Zi Tan¹, Samir Benlekbir¹, Hong Cui¹, Tiantian Zhao⁴, Gregory A. Wasney^{1,5}, Patrick Budylowski^{6,7}, Furkan Guvenc^{6,8}, Jocelyn C. Newton¹, Taylor Sicard^{1,2}, Anthony Semesi¹, Krithika Muthuraman¹, Amy Nouanesengsy^{1,2}, Katherine Prieto¹, Stephanie A. Bueler¹, Sawsan Youssef⁹, Sindy Liao-Chan⁹, Jacob Glanville⁹, Natasha Christie-Holmes⁶, Samira Mubareka^{10,11}, Scott D. Gray-Owen⁸, John L. Rubinstein^{1,2,12}, Bebhinn Treanor^{4,13,14}, Jean-Philippe Julien^{1,2,4}

Correspondence to: jean-philippe.julien@sickkids.ca

This PDF file includes:

Materials and Methods
Figs. S1 to S8
Tables S1 to S7

Materials and Methods

Protein expression and purification

Genes encoding VHH-human apoferritin fusion, Fc fusions, Fabs, IgG, and RBD mutants were synthesized and cloned by GeneArt (Life Technologies) into the pcDNA3.4 expression vector. All constructs were expressed transiently in HEK293F cells (Thermo Fisher Scientific) at a density of 0.8×10^6 cells/mL with 50 µg of DNA per 200 mL of cells using FectoPRO (Polyplus Transfections) in a 1:1 ratio unless specified otherwise. After 6-7 days of incubation at 125 rpm oscillation at 37° C, 8% CO₂, and 70% humidity in a Multitron Pro shaker (Infors HT), cell suspensions were harvested by centrifugation at 5000 ×g for 15 min and supernatants were filtered through a 0.22 µm Steritop filter (EMD Millipore). Fabs and IgGs were transiently expressed by co-transfected 90 µg of the LC and the HC in a 1:2 ratio and purified using KappaSelect affinity column (GE Healthcare) and HiTrap Protein A HP column (GE Healthcare), respectively with 100 mM glycine pH 2.2 as the elution buffer. Eluted fractions were immediately neutralized with 1 M Tris-HCl, pH 9.0 and further purified using a Superdex 200 Increase size exclusion column (GE Healthcare). Fc fusions of ACE2 and VHH-72 were purified the same way as IgGs. The VHH-72 apoferritin fusion was purified by hydrophobic interaction chromatography using a HiTrap Phenyl HP column and the eluted fraction was loaded onto a Superose 6 10/300 GL size exclusion column (GE Healthcare) in 20 mM sodium phosphate pH 8.0, 150 mM NaCl. The prefusion S ectodomain (BEI NR52394), wild type RBD (BEI NR52309) and mutant RBDs were purified using a HisTrap Ni-NTA column (GE Healthcare) followed by Superose 6 and Superdex 200 Increase size exclusion columns (GE Healthcare), respectively in 20 mM phosphate pH 8.0, 150 mM NaCl buffer.

Design, expression and purification of split Multabodies

Genes encoding scFab and scFc fragments linked to half apoferritin were generated by deletion of residues 1 to 95 (C-Ferritin) and 95 to 175 (N-Ferritin) of the light chain of human apoferritin using the KOD-Plus mutagenesis kit (Toyobo, Osaka, Japan). Transient transfection of the split Multabodies in HEK 293F cells were obtained by mixing 66 µg of the plasmids scFab-human apoferritin: scFc-human N-Ferritin: scFab-C-Ferritin in a 2:1:1 ratio. In the case of multispecific Multabodies, a 4:2:1:1 ratio of scFab1-human apoferritin: scFc-human N-Ferritin: scFab2-C-Ferritin: scFab3-C-Ferritin was used. The DNA mixture was filtered and incubated at RT with 66 µl of FectoPRO before adding to the cell culture. Split Multabodies were purified by affinity chromatography using a HiTrap Protein A HP column (GE Healthcare) with 20 mM Tris pH 8.0, 3 M MgCl₂ and 10% glycerol elution buffer. Fractions containing the protein were concentrated and further purified by gel filtration on a Superose 6 10/300 GL column (GE Healthcare).

Negative-stain electron microscopy

3 µL of Multobody at a concentration approximately of 0.02 mg/mL was placed on the surface of a carbon-coated copper grid that had previously been glow-discharged in air for 15 sec, allowed to adsorb for 30 s, and stained with 3 µL of 2% uranyl formate. Excess stain was removed immediately from the grid using Whatman No. 1 filter paper and an additional 3 µL of 2% uranyl formate was added for 20 s. Grids were imaged with a FEI Tecnai T20 electron microscope operating at 200 kV and equipped with an Orius charge-coupled device (CCD) camera (Gatan Inc).

Biolayer interferometry

Direct binding kinetics measurements were conducted using an Octet RED96 BLI system (Sartorius ForteBio) in PBS pH 7.4, 0.01% BSA and 0.002% Tween at 25° C. His-tagged RBD or SARS-CoV-2 Spike protein was loaded onto Ni-NTA (NTA) biosensors (Sartorius ForteBio) to

reach a BLI signal response of 0.8 nm. Association rates were measured by transferring the loaded biosensors to wells containing a 2-fold dilution series from 250 to 16 nM (Fabs), 125 to 4 nM (IgG), and 16 to 0.5 nM (MB). Dissociation rates were measured by dipping the biosensors into buffer-containing wells. The duration of each of these two steps was 180 s. Fc characterization in the split Multobody design was assessed by measuring binding to hFc γ RI and hFcRn. To probe the theoretical capacity of the Multabodies to undergo endosomal recycling, binding to the hFcRn β 2-microglobulin complex was measured at physiological (7.5) and endosomal (5.6) pH. Competition assays were performed in a two-step binding process. Ni-NTA biosensors preloaded with His-tagged RBD were first dipped into wells containing the primary antibody at 50 μ g/mL for 180 s. After a 30 s baseline period, the sensors were dipped into wells containing the second antibody at 50 μ g/ml for an additional 300 s.

Dynamic light scattering

The hydrodynamic radius (R_h) of the Multobody was determined by dynamic light scattering (DLS) using a DynaPro Plate Reader III (Wyatt Technology). 20 μ L of the Multobody at a concentration of 1 mg/mL was added to a 384-well black, clear bottom plate (Corning) and measured at a fixed temperature of 25° C with a duration of 5 s per read. Particle size determination and polydispersity were obtained from the accumulation of 5 reads using the Dynamics software (Wyatt Technology).

Aggregation temperature measurements

Aggregation temperature (T_{agg}) of the Multabodies and parental IgGs were determined using a UNit instrument (Unchained Labs). Samples were concentrated to 1.0 mg/mL and subjected to a thermal ramp from 25 to 95° C with 1° C increments. T_{agg} was determined as the temperature at which 50% increase in the static light scattering at a 266 nm wavelength relative to baseline was

observed (i.e. the maximum value of the differential curve). The average and the standard error of two independent measurements were calculated using the UNit analysis software.

Pharmacokinetics and immunogenicity studies

A surrogate Multabody composed of the scFab and scFc fragments of mouse HD37 (anti-hCD19) IgG2a fused to the N-terminus of the light chain of mouse apoferritin (mFerritin) was used for the study. HD37 scFab-mFerritin: Fc-mFerritin: mFerritin in a 2:1:1 ratio was transfected and purified following the procedure described above. L234A, L235A and P329G mutations were introduced in the mouse IgG2a Fc-construct to silence effector functions of the Multabody⁴³. *In vivo* studies were performed using 12-week-old male C57BL/6 mice purchased from Charles River (Strain code: 027), housed in individually-vented cages. All procedures were approved by the Local Animal Care Committee at the University of Toronto Scarborough. A single injection of approximately 5 mg/kg of Multabodies or control samples (HD37 IgG -IgG1 and IgG2a subtypes) and *Helicobacter pylori* ferritin (hpFerritin)-PfCSP malaria peptide in 200 µL of PBS (pH 7.5) were subcutaneously injected. Blood samples were collected at multiple time points and serum samples were assessed for levels of circulating antibodies and anti-drug antibodies (ADA) by ELISA. Briefly, 96-well Pierce Nickel Coated Plates (Thermo Fisher) were coated with 50 µL at 0.5 µg/ml of the His_{6x}-tagged antigen hCD19 to determine circulating HD37-specific concentrations using reagent-specific standard curves for IgGs and Multabodies. For ADA determination, Nunc MaxiSorp plates (Biolegend) were coated with a 12-mer HD37 scFab-mFerritin or with the hpFerritin-PfCSP malaria peptide. HRP-ProteinA (Invitrogen) was used as a secondary molecule and the chemiluminescence signal was quantified using a Synergy Neo2 Multi-Mode Assay Microplate Reader (Biotek Instruments).

Biodistribution studies

8-week-old BALB/c mice were purchased from The Jackson Laboratory and housed in individually-vented caging. All procedures were approved by the Local Animal Care Committee at the University of Toronto. The HD37 IgG2a Multabody or HD37 IgG2a control were fluorescently conjugated with Alexa-647 using an Alexa FluorTM 647 Antibody Labeling kit (Invitrogen) as per manufacturer instructions. PerkinElmer IVIS Spectrum (PerkinElmer) was used to conduct non-invasive biodistribution experiments. BALB/c mice were injected subcutaneously into the loose skin over the shoulders with approximately 5 mg/kg of the MB or control samples in 200 µL of PBS (pH 7.5) and imaged at time 0, 1h, 6h, 24h, 2d, 3d, 4d, 8d, 11d following injection. Prior to imaging, mice were placed in an anesthesia induction chamber containing a mixture of isoflurane and oxygen for 1 min. Anesthetized mice were then placed in the prone position at the center of a built-in heated docking system within the IVIS imaging system (maintained at 37°C and supplied with a mixture of isoflurane and oxygen). For whole body 2D imaging, mice were imaged for 1-2 s (excitation 640 nm, emission 680 nm) inside the imaging system. Data were analyzed and reconstructed with the IVIS software (Living Image Software for IVIS) using 640 nm/680 nm laser.

Panning of Phage libraries against the RBD of SARS-CoV-2

143 healthy human subjects were used for the assembly of a SuperHuman 2.0 library. CDR-H3 diversity was sourced by PCR from naive CD27-IgM+ B-cells while other CDR diversity was sourced from CD27+IgG+ B cells from the therapeutic frameworks IGHV1-46, IGHV1-69, IGHV3-15, IGHV3-23, IGKV1-39, IGKV2-28, IGKV3-15 and IGKV4-1 by using PCR overlap extension. The light and heavy chains were transformed to exceed 1e⁸ and 7.6e¹⁰ transformants for each chain framework, respectively. Illumina MiSeq replicate rarefaction analysis was used to assure a recovery of over 98% unique clones. In addition, Protein L and Protein A were used (10

min incubation at 70° C) to select thermostable and well-expressing light chain diversity. The EXPi-293 mammalian expression system was used for expression of the receptor Binding domain (RBD)-Fc-Avi tag construct of the SARS-CoV-2. This protein was subsequently purified by protein G Dynabeads, biotinylated and quality-controlled for biotinylation and binding to ACE2 recombinant protein (Sino Biologics Inc). The SuperHuman 2.0 Phage library (5×10^{12}) was heated for 10 min at 72° C and de-selected against Protein G DynabeadsTM (Invitrogen), M-280 Streptavidin DynabeadsTM (Invitrogen), Histone from Calf Thymus (Sigma), Human IgG (Sigma) and ssDNA-Biotin NNK from Integrated DNA Technologies and DNA-Biotin NNK from Integrated DNA Technologies. Next, the library was panned against the RBD-captured by M-280 Streptavidin DynabeadsTM using an automated protocol on Kingfisher FLEX (Thermofisher). Selected phages were acid eluted from the beads and neutralized using Tris-HCl pH 7.9 (Teknova). ER2738 cells were infected with the neutralized phage pools at OD₆₀₀=0.5 at a 1:10 ratio and after 40 min incubation at 37° C and 100 rpm, the phage pools were centrifuged and incubated on agar with antibiotic selection overnight at 30° C. The rescued phages were precipitated by PEG and subjected to three additional rounds of soluble-phase automated panning. PBST/1% BSA buffer and/or PBS/1% BSA was used in the de-selection, washes and selection rounds.

Screening of anti-SARS-CoV-2 scFvs in bacterial periplasmic extracts with SARS-CoV-2 RBD

Anti-SARS-CoV-2 RBD scFvs selected from phage display were expressed and screened using high-throughput surface plasmon resonance (SPR) on Carterra LSA Array SPR instrument (Carterra) equipped with HC200M sensor chip (Carterra) at 25° C. A V5 epitope tag was added to the scFv to enable capture via immobilized anti-V5 antibody (Abcam, Cambridge, MA) that was pre-immobilized on the chip surface by standard amine-coupling. Briefly: the chip surface was

first activated by 10 min injection of a 1:1:1 (v/v/v) mixture of 0.4 M 1-Ethyl-3-(3-Dimethylaminopropyl) carbodiimide hydrochloride (EDC), 0.1 M N-hydroxysulfosuccinimide (sNHS) and 0.1 M 2-(N-morpholino) ethanesulfonic acid (MES) pH 5.5. Then, 50 µg/ml of anti-V5 tag antibody prepared in 10 mM sodium acetate pH 4.3 was coupled for 14 min and the excess reactive esters were blocked with 1 M ethanolamine HCl pH 8.5 during a 10 min injection. For screening, a 384-ligand array comprising of crude bacterial periplasmic extracts (PPE) containing the scFvs (1 spot per scFv) was prepared. Each extract was prepared at a 2-fold dilution in running buffer (10 mM HEPES pH 7.4, 150 mM NaCl, 3 mM EDTA, 0.01% (v/v) Tween-20 (HBSTE)) and printed on the anti-V5 surface for 15 min. SARS-CoV-2 RBD Avi Tev His tagged was then prepared at 0, 3.7, 11.1, 33.3, 100, 37, and 300 nM in 10 mM HEPES pH 7.4, 150 mM NaCl, 0.01% (v/v) Tween-20 (HBST) supplemented with 0.5 mg/ml BSA and injected as analyte for 5 min with a 15 min dissociation time. Samples were injected in ascending concentration without any regeneration step. Binding data from the local reference spots was used to subtracted signal from the active spots and the nearest buffer blank analyte responses were subtracted to double-reference the data. The double-referenced data were fitted to a simple 1:1 Langmuir binding model in Carterra's Kinetic Inspection Tool (version Oct. 2019). 20 medium-affinity binders from phage display screening were selected for the present study.

Virus production and pseudovirus neutralization assays

SARS-CoV-2 pseudotyped viruses (PsV) were generated using an HIV-based lentiviral system as previously described⁴⁴ with few modifications. Briefly, 293T cells were co-transfected with a lentiviral backbone encoding the luciferase reporter gene (BEI NR52516), a plasmid expressing the Spike (BEI NR52310) and plasmids encoding the HIV structural and regulatory proteins Tat (BEI NR52518), Gag-pol (BEI NR52517) and Rev (BEI NR52519). 24 h post transfection at 37°

C, 5 mM sodium butyrate was added to the media and the cells were incubated for an additional 24-30 h at 30° C. SARS-CoV-2 Spike mutant D614G was kindly provided by D.R. Burton (The Scripps Research Institute) and the rest of the PsV mutants were generated using the KOD-Plus mutagenesis kit (Toyobo, Osaka, Japan). Neutralization was determined in a single-cycle neutralization assay using 293T-ACE2 cells (BEI NR52511) and HeLa-ACE2 cells (kindly provided by D.R. Burton; The Scripps Research Institute). PsV neutralization was monitored by adding Britelite plus reagent (PerkinElmer) to the cells and measuring luminescence in relative light units (RLUs) using a Synergy Neo2 Multi-Mode Assay Microplate Reader (Biotek Instruments). IC₅₀ fold increase was calculated as: IgG_{IC50}(μg/mL) / MB_{IC50}(μg/mL). Two to three biological replicates with two technical replicates each were performed.

Authentic virus neutralization assays

VeroE6 cells were seeded in a 96F plate at a concentration of 30,000/well in DMEM supplemented with 100U Penicillin, 100U Streptomycin and 10% FBS. Cells were allowed to adhere to the plate and rest overnight. After 24 h, 5-fold serial dilutions of the IgG and MB samples were prepared in DMEM supplemented with 100U Penicillin and 100U Streptomycin in a 96R plate in quadruplicates (25 uL/well). 25 uL of SARS-CoV-2/SB2-P4-PB⁴⁵ Clone 1 was added to each well at 100TCID/well and incubated for 1 h at 37 °C with shaking every 15 min. After co-culturing, the media from the VeroE6 plate was removed, and 50 uL antibody-virus sample was used to inoculate VeroE6 cells in quadruplicates for 1 h at 37 °C, 5% CO₂, shaking every 15 min. After 1 h inoculation, the inoculum was removed and 200 uL of fresh DMEM supplemented with 100U Penicillin, 100U Streptomycin and 2% FBS was added to each well. The plates were further incubated for 5 days. The cytopathic effect (CPE) was monitored and PRISM was used to calculate IC₅₀ values. Three biological replicates with four technical replicates each were performed.

Cross-linking of Spike protein with Fabs 80, 298 and 324

100 µg of Spike trimer was mixed with 2x molar excess of Fab 80, 298 or 324 in 20 mM HEPES pH 7.0, 150 mM NaCl. Proteins were crosslinked by addition of 0.075% (v/v) glutaraldehyde (Sigma Aldrich) and incubated at room temperature for 120 min. Complexes were purified via size exclusion chromatography (Superose6 Increase 10/300 GL, GE Healthcare), concentrated to 0.5 mg/mL and directly used for cryo-EM grid preparation.

Cross-linking of Fab 46-RBD complex

100 µg of Fab 46 was mixed with 2x molar excess of RBD in 20 mM HEPES pH 7.0, 150 mM NaCl. The complex was crosslinked by addition of 0.05% (v/v) glutaraldehyde (Sigma Aldrich) and incubated at room temperature for 45 min. The cross-linked complex was purified via size exclusion chromatography (Superdex 200 Increase 10/300 GL, GE Healthcare), concentrated to 2.0 mg/ml and directly used for cryo-EM grid preparation.

Cryo-EM data collection and image processing

3 µl of sample was deposited on holey gold grids prepared in-house⁵¹, which were glow-discharged in air for 15 s with a PELCO easiGlow (Ted Pella) before use. Sample was blotted for 6 s with a modified FEI Mark III Vitrobot (maintained at 4° C and 100% humidity) using an offset of -5, and subsequently plunge-frozen in a mixture of liquid ethane and propane. Data was acquired at 300 kV with a Thermo Fisher Scientific Titan Krios G3 electron microscope and prototype Falcon 4 camera operating in electron counting mode at 250 frames/s. Movies were collected for 9.6 s with 29 exposure fractions, a camera exposure rate of ~5 e⁻/pix/s, and total specimen exposure of ~44 e⁻/Å². No objective aperture was used. The pixel size was calibrated at 1.03 Å/pixel from a gold diffraction standard. The microscope was automated with the *EPU* software package and data collection was monitored with *cryoSPARC Live*⁵².

To overcome preferred orientation encountered with some of the samples, tilted data collection was employed⁵³. For the Spike-Fab 80 complex, 820 0° tilted movies and 2790 40° tilted movies were collected. For the Spike-Fab 298 complex, 4259 0° tilted movies and 3513 40° tilted movies were collected. For the Spike-Fab 324 complex, 1098 0° tilted movies and 3380 40° tilted movies were collected. For the RBD-Fab 46 complex, 4722 0° tilted movies were collected. For 0° tilted movies, cryoSPARC patch motion correction was performed. For 40° tilted movies, *Relion* MotionCorr^{54,55} was used. Micrographs were then imported into *cryoSPARC* and patch CTF estimation was performed. Templates generated from 2D classification during the *cryoSPARC Live* session were used for template selection of particles. 2D classification was used to remove junk particle images, resulting in a dataset of 80,951 particle images for the Spike-Fab 80 complex, 203,138 particle images for the Spike-Fab 298 complex, 64,365 particle images for the Spike-Fab 324 complex, and 2,143,629 particle images for the RBD-Fab 46 complex. Multiple rounds of multi-class *ab initio* refinement were used to clean-up the particle image stacks, and homogeneous refinement was used to obtain consensus structures. For tilted particles, particle polishing was done within *Relion* at this stage and re-imported back into *cryoSPARC*. For the Spike-Fab complexes, extensive flexibility was observed. 3D variability analysis was performed⁵⁶ and together with heterogeneous refinement used to classify out the different states present. Non-uniform refinement was then performed on the final set of particle images⁵⁷. For the RBD-Fab 46 complex, *cryoSPARC ab initio* refinement with three classes was used iteratively to clean up the particle image stack. Thereafter, the particle image stack with refined Euler angles was brought into *cisTEM* for reconstruction⁵⁸ to produce a 4.0 Å resolution map. Transfer of data between *Relion* and *cryoSPARC* was done with *pyem*⁵⁹.

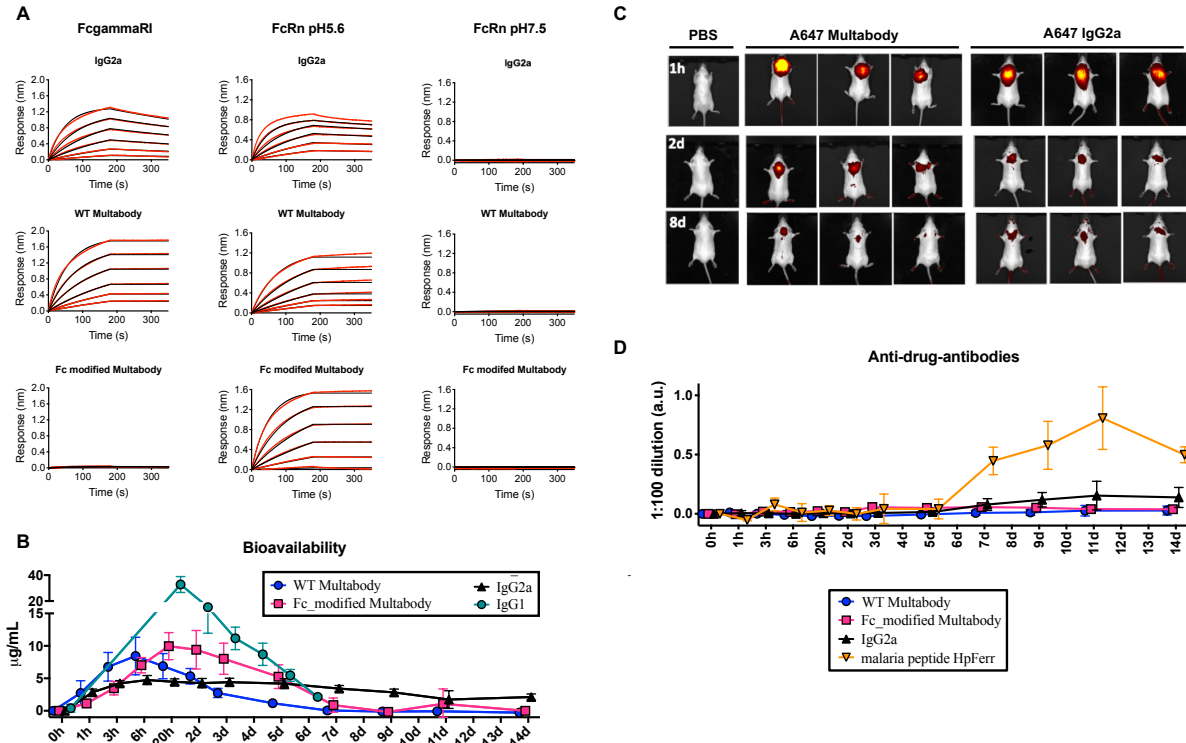
Crystallization and structure determination

A ternary complex of 52 Fab-298 Fab-RBD was obtained by mixing 200 µg of RBD with 2X molar excess of each Fab in 20 mM TRIS pH 8.0, 150 mM NaCl and subsequently purified via size exclusion chromatography (Superdex 200 Increase 10/300 GL, GE Healthcare). Fractions containing the complex were concentrated to 7.3 mg/ml and mixed in a 1:1 ratio with 20% (w/v) 2-propanol, 20% (w/v) PEG 4000, 0.1 M sodium citrate pH 5.6. Crystals appeared after ~1 day and were cryoprotected in 10% (v/v) ethylene glycol before being flash-frozen in liquid nitrogen. Data were collected on the 23-ID-D beamline at the Argonne National Laboratory Advanced Photon Source. The dataset was processed using XDS and XPREP⁴⁶. Phases were determined by molecular replacement using Phaser⁴⁷ with CNT088 Fab as a model for 52 Fab (PDB ID: 4DN3), 20358 Fab as a model for 298 Fab (PDB ID: 5CZX), and PDB ID: 6XDG as a search model for the RBD. Refinement of the structure was performed using phenix.refine⁴⁸ and iterations of manual building and refinement in Coot⁴⁹. Access to all software was supported through SBGrid⁵⁰.

46. Kabsch, W. *et al.* *XDS. Acta Crystallogr. Sect. D Biol. Crystallogr.* **66**, 125–132 (2010).
47. McCoy, A. J. *et al.* Phaser crystallographic software. *J. Appl. Crystallogr.* **40**, 658–674 (2007).
48. Adams, P. D. *et al.* PHENIX: A comprehensive Python-based system for macromolecular structure solution. *Acta Crystallogr. Sect. D Biol. Crystallogr.* **66**, 213–221 (2010).
49. Emsley, P., Lohkamp, B., Scott, W. G. & Cowtan, K. Features and development of Coot. *Acta Crystallogr. Sect. D Biol. Crystallogr.* **66**, 486–501 (2010).
50. Morin, A. *et al.* Collaboration gets the most out of software. *Elife* **2**, (2013).
51. Marr, C. R., Benlekbir, S. & Rubinstein, J. L. Fabrication of carbon films with ~500nm holes for cryo-EM with a direct detector device. *J. Struct. Biol.* **185**, 42–47 (2014).

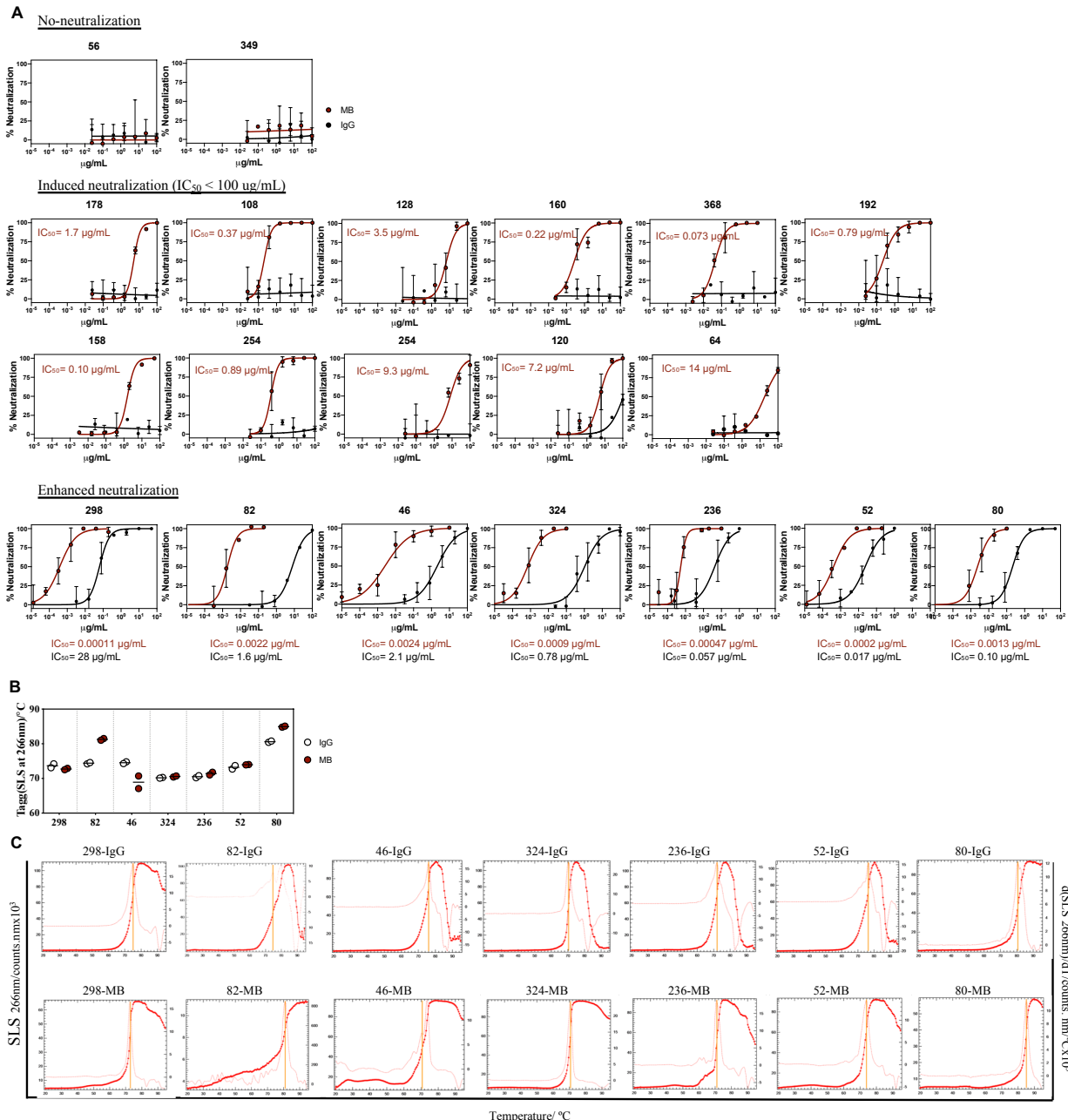
52. Punjani, A., Rubinstein, J. L., Fleet, D. J. & Brubaker, M. A. CryoSPARC: Algorithms for rapid unsupervised cryo-EM structure determination. *Nat. Methods* **14**, 290–296 (2017).
53. Zi Tan, Y. *et al.* Addressing preferred specimen orientation in single-particle cryo-EM through tilting. *Nat. Methods* **14**, (2017).
54. Zivanov, J. *et al.* New tools for automated high-resolution cryo-EM structure determination in RELION-3. *Elife* **9**, e42166 (2018).
55. Scheres, S. H. W. RELION: Implementation of a Bayesian approach to cryo-EM structure determination. *J. Struct. Biol.* **180**, 519–530 (2012).
56. Punjani, A. & Fleet, D. 3D Variability Analysis: Directly resolving continuous flexibility and discrete heterogeneity from single particle cryo-EM images. *bioRxiv* (2020).
57. Punjani, A., Zhang, H. & Fleet, D. Non-uniform refinement: Adaptive regularization improves single particle cryo-EM reconstruction. *bioRxiv* (2019).
58. Grant, T., Rohou, A. & Grigorieff, N. CisTEM, user-friendly software for single-particle image processing. *Elife* **7**, e35383 (2018).
59. Asarnow, D., Palovcak, E. & Cheng, Y. asarnow/pyem: UCSF pyem v0. 5. (2019).

Fig. S1.



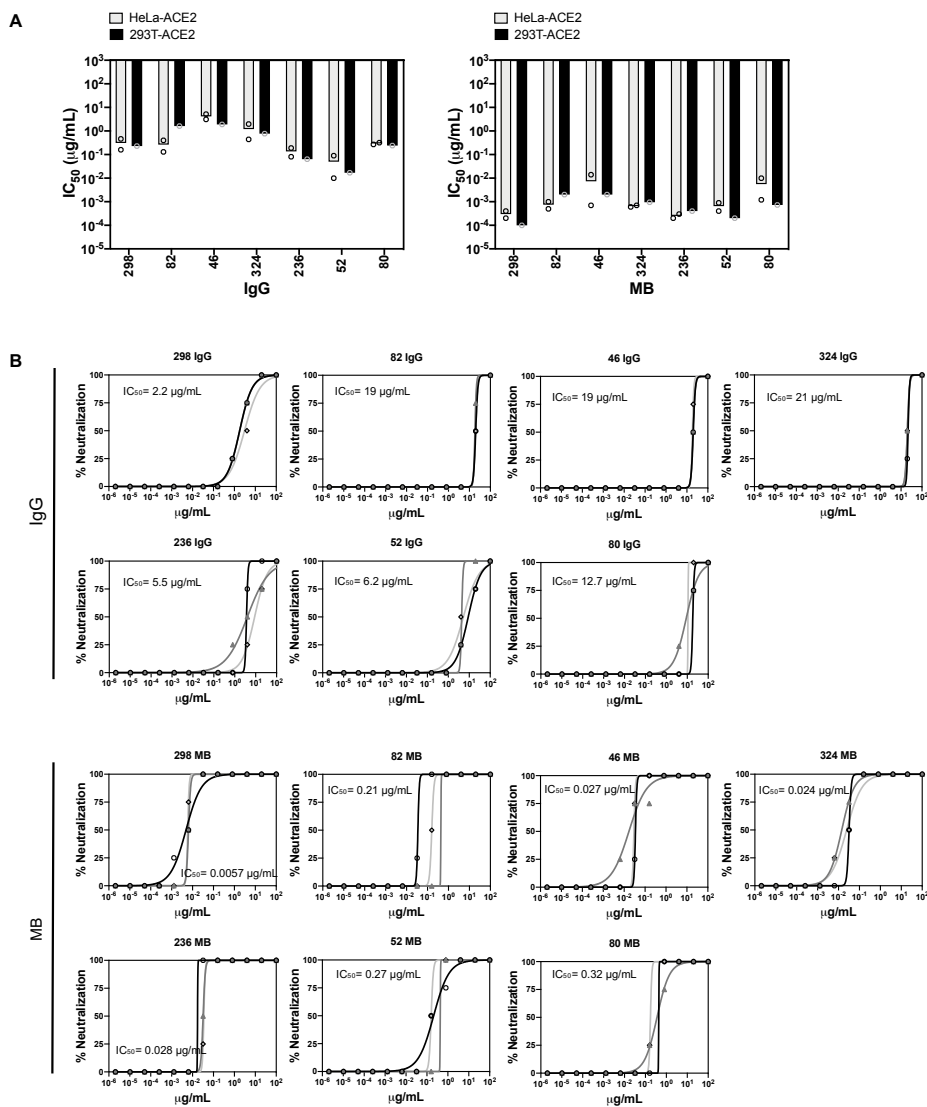
Bioavailability, biodistribution and immunogenicity of a surrogate Multabody in mice. (A) Binding kinetics of WT and Fc-modified (LALAP mutation) MB to mouse Fc γ RI (left) and mouse FcRn at endosomal (middle) and physiological (right) pH in comparison to the parental IgG. 2-fold dilution series from 100 to 3 nM (IgG), and 10 to 0.3 nM (MB) were used. Black lines represent raw data whereas red lines represent global fits. (B) Five male C57BL/6 mice per group were used to assess the serum concentration of a surrogate mouse MB, a Fc-modified MB (LALAP mutation) and parental mouse IgGs (IgG1 and IgG2a subtype) after subcutaneous administration of 5 mg/kg. (C) MB and IgG2a samples were labeled with Alexa-647 for visualization of their biodistribution post subcutaneous injection into three BALB/c mice/group via live non-invasive 2D whole body imaging. (D) Five male C57BL/6 mice per group were used to assess any anti-drug antibody response induced by the mouse surrogate Multabody in comparison to parental IgG and a species-mismatched malaria PfCSP peptide fused to *Helicobacter pylori* ferritin (HpFerr).

Fig. S2.



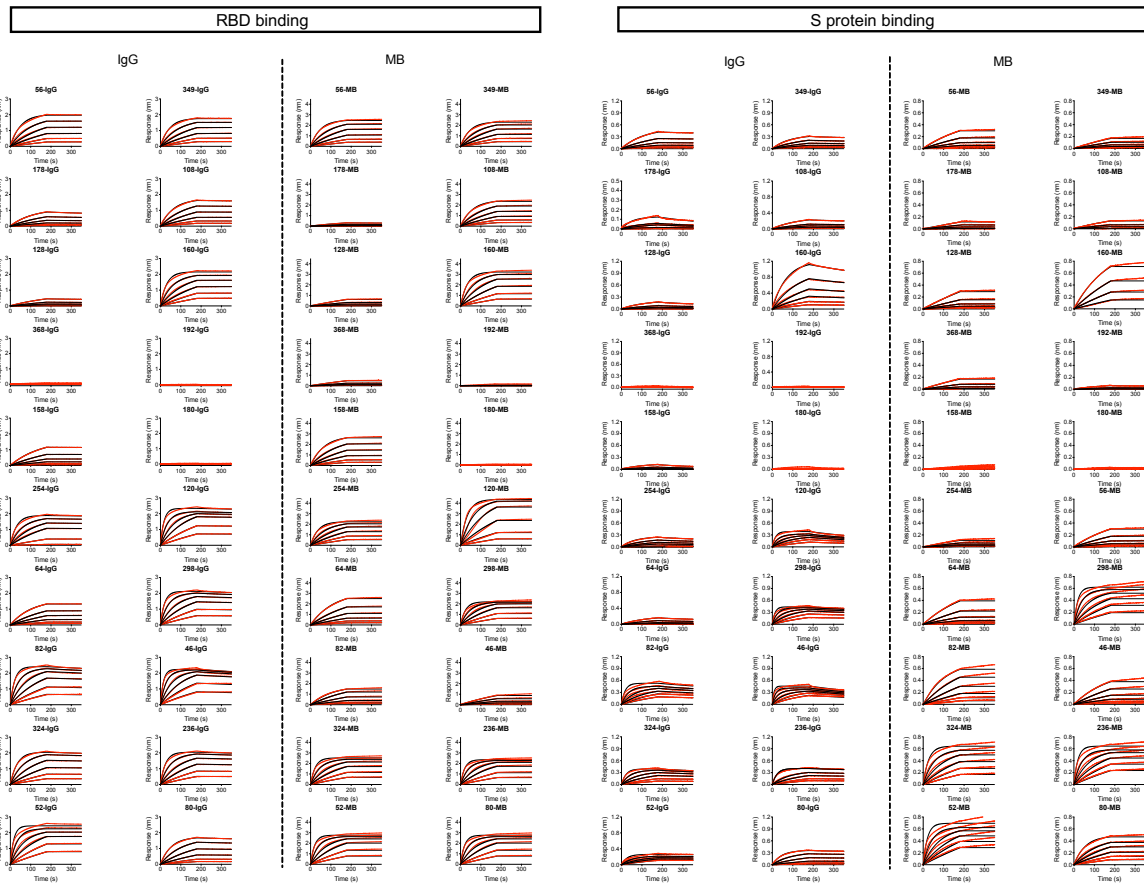
Neutralization and thermostability of SARS-CoV-2 RBD-targeting Multabodies and their parental IgGs. (A) Representative neutralization titration curves of 20 antibodies against SARS-CoV-2 PsV when displayed as IgGs (black) and MBs (dark red). The mean IC_{50} value of three biological replicates, each with two technical replicates are displayed for comparison. **(B)** Comparison of the aggregation temperature (T_{agg}) of the seven most potent IgGs (white) and their respective MBs (dark red). **(C)** Static light scattering (SLS) at 266 nm versus temperature plots (dark red) from (b). T_{agg} values are calculated from the maximum of the differential curves (light red) and indicated with yellow lines.

Fig. S3.



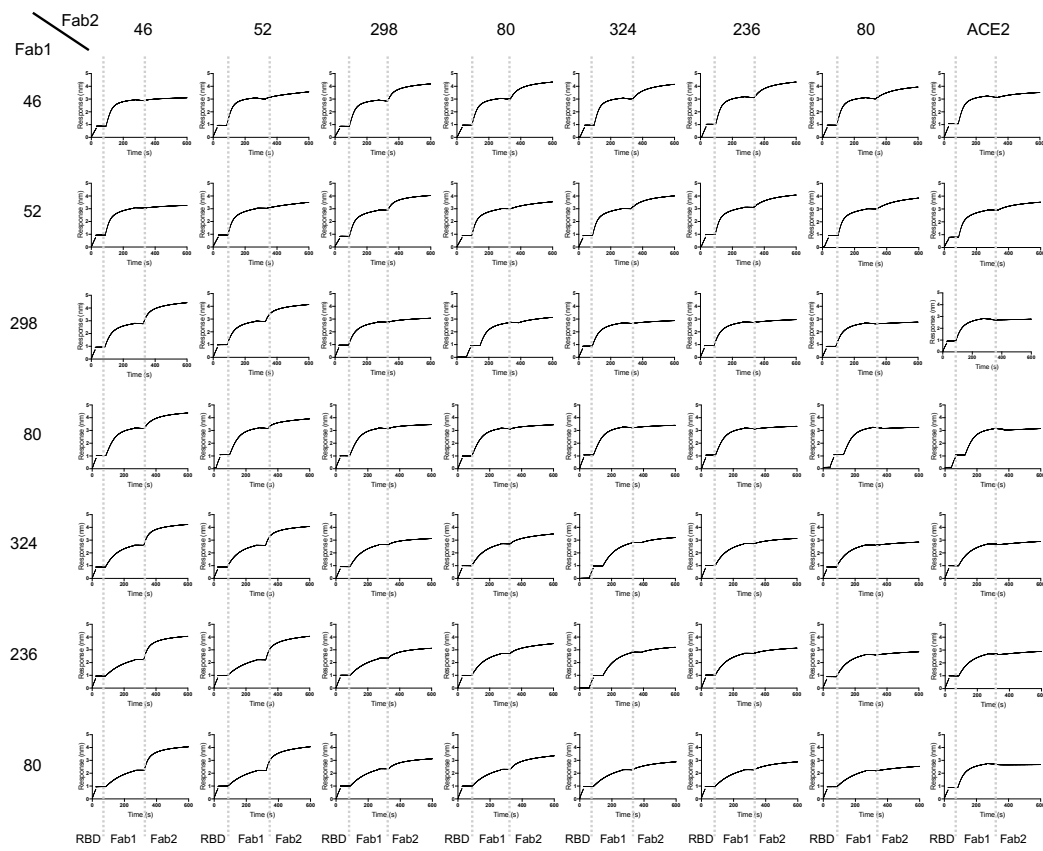
Neutralization profiles of selected IgGs and MBs in different assays. (A) Similar neutralization profiles of IgGs (left) vs MBs (right) against pseudotyped SARS-CoV-2 PsV targeting 293T-ACE2 (black) and HeLa-ACE2 (gray) target cells. The mean IC_{50} value and individual IC_{50} values of three and two biological replicates are shown for 293T-ACE2 and HeLa-ACE2 cells, respectively. (B) Neutralization titration curves of three biological replicates (different shades of gray) against the authentic SARS-CoV-2/SB2-P4-PB strain⁴⁵. The mean IC_{50} is indicated. The less sensitive neutralization phenotype observed against authentic virus in comparison to PsV is in agreement with previous reports^{5,13,14,17}. However, other studies have observed similar values^{3,11,12,16} between the two assays. This discrepancy makes cross-comparison of antibody potencies against live replicating virus difficult and is likely due to differences in the length of time of the neutralization experiment. Short incubation times will minimize the number of replications that the virus can undergo, resembling the one replication cycle of the PsV assays.

Fig. S4.



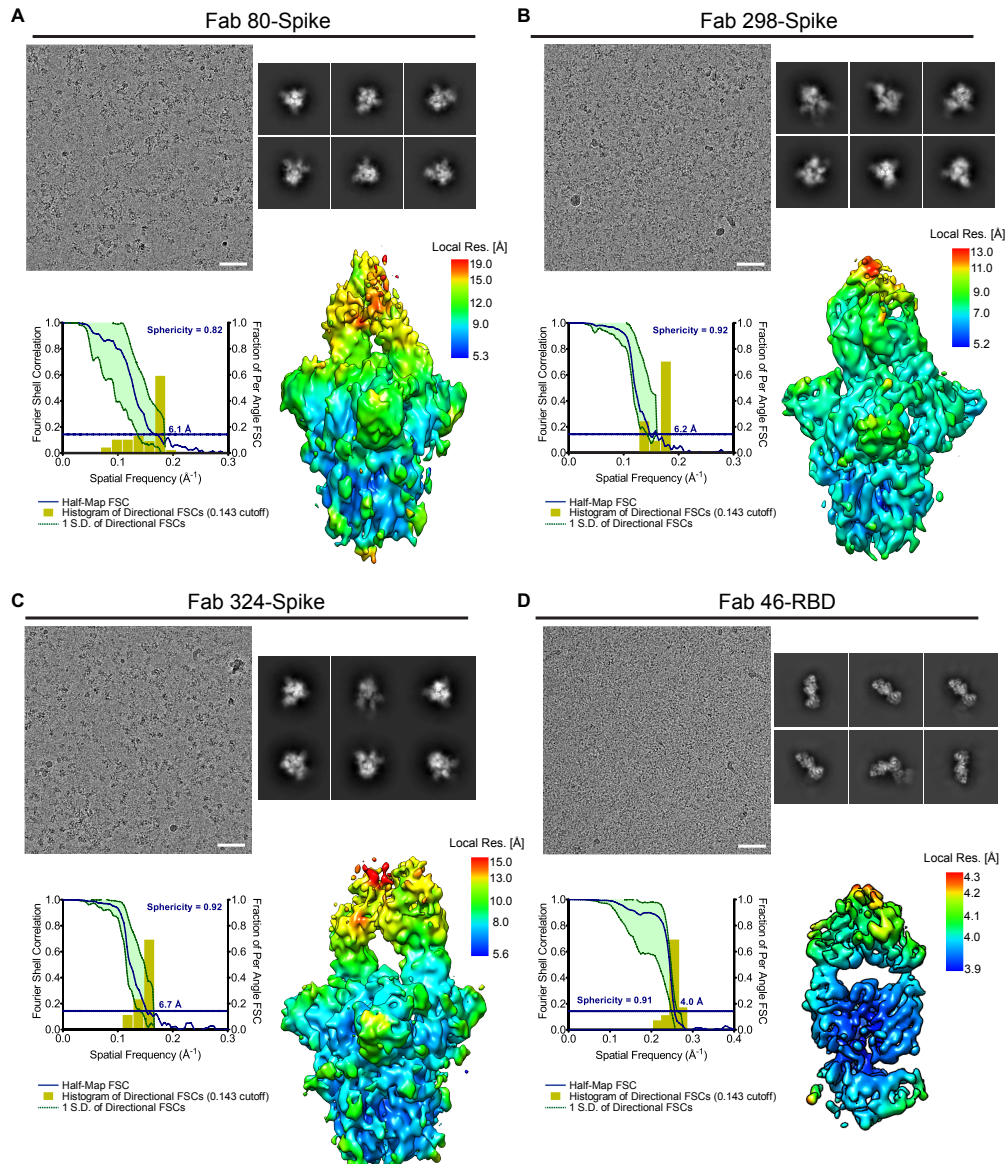
Binding profiles of IgGs and MBs. BLI response curves of IgG and MBs binding to RBD (left) and S protein (right) of SARS-CoV-2 immobilized onto Ni-NTA biosensors. 2-fold dilution series from 125 to 4 nM (IgG), and 16 to 0.5 nM (MB) were used. Black lines represent raw data whereas red lines represent global fits.

Fig. S5.



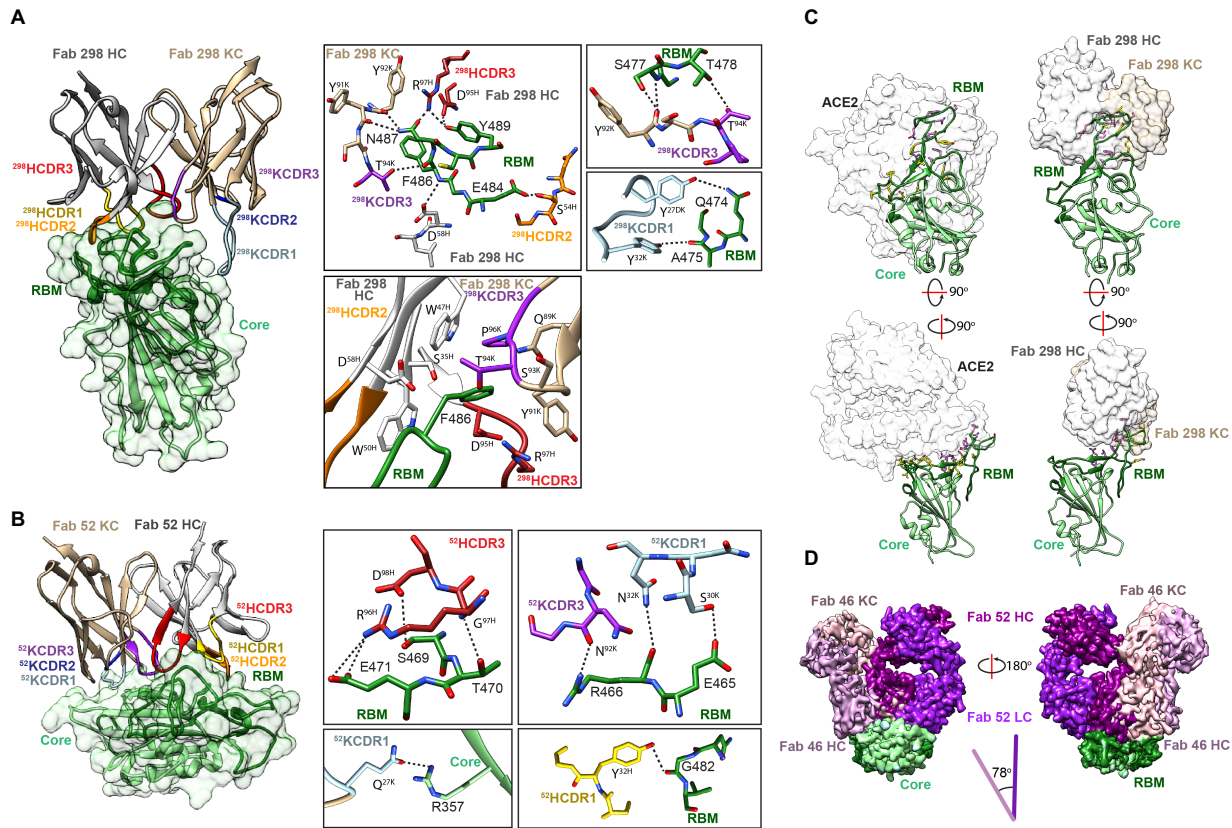
Epitope binning. mAb binding competition experiments to His-tagged RBD as measured by biolayer interferometry (BLI). 50 µg/ml of mAb 1 was incubated for 3 min followed by incubation with 50 µg/ml of mAb 2 for 5 min.

Fig. S6.



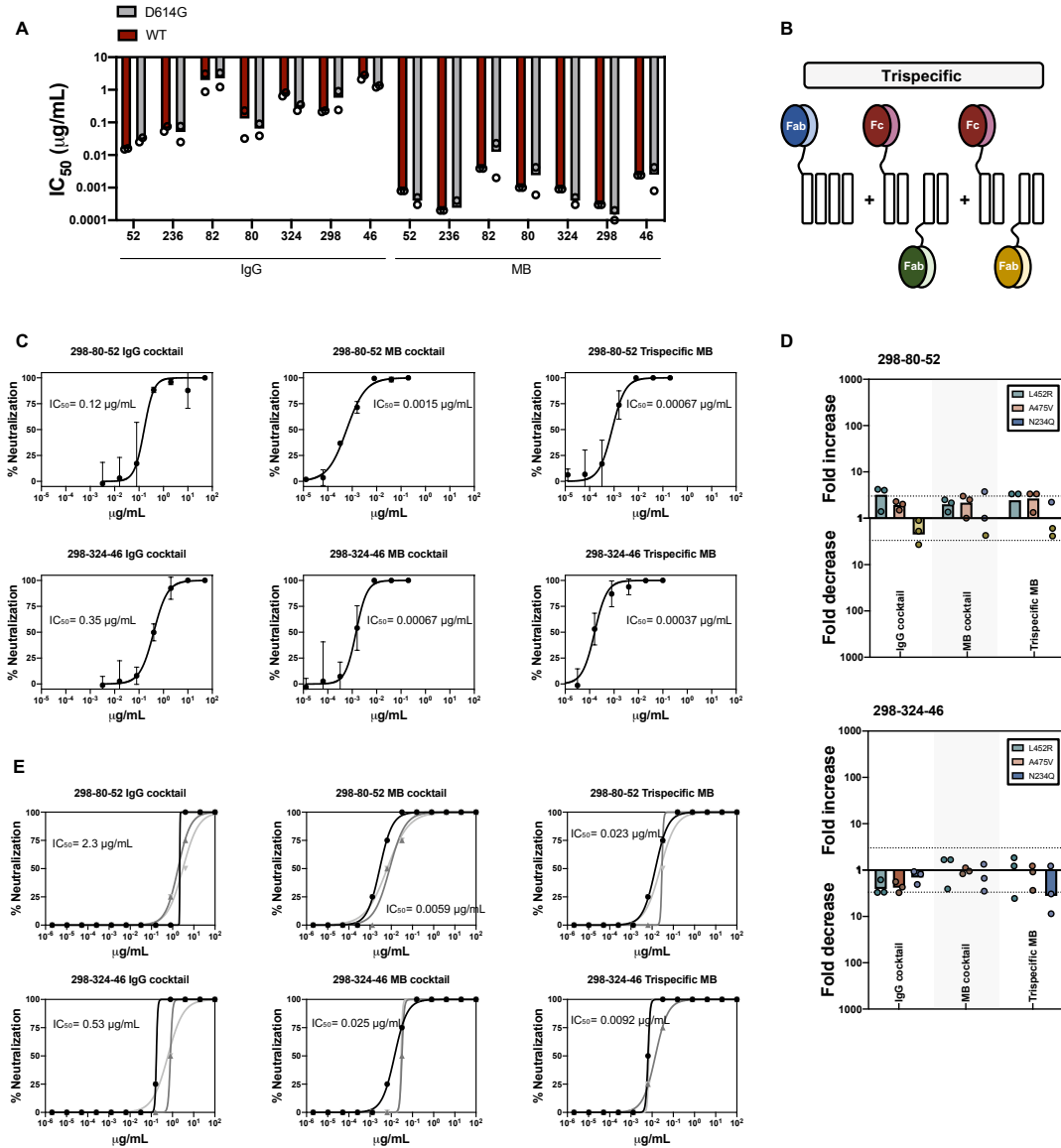
Cryo-EM analysis of the Fab-Spike and Fab-RBD complexes. Representative cryo-EM micrograph (Scale bar 50 nm, top left), selected 2D class averages (top right), Fourier shell correlation curve from the final 3D non-uniform refinement (bottom left) and local resolution (\AA) plotted on the surface of the cryo-EM map (bottom right) are shown for the Fab 80-Spike complex (A), the Fab 298-Spike complex (B), the Fab 324-Spike complex (C), and the Fab 46-RBD complex (D).

Fig. S7.



Binding interfaces of mAbs 52 and 298 and the RBD. Interaction of mAbs 298 (**A**) and 52 (**B**) with RBD (light and dark green for the core and RBM regions, respectively) is mediated by complementarity determining regions (CDR) heavy (H) 1 (yellow), H2 (orange), H3 (red), kappa light (K) 1 (light blue) and K3 (purple) (left panels). Critical binding residues are shown in sticks (right panels). H-bonds and salt bridges are depicted as black dashed lines. L and H chains of Fabs are shown in tan and white, respectively. (**C**) Bottom and side views of ACE2 (left) and Fab 298 (right) bound to RBD. RBD side-chains that are part of the binding interface of the ACE2-RBD and Fab 298-RBD complexes are depicted in pink, while RBD side-chains unique to a given interface are shown in yellow. Surfaces of ACE2, variable regions of Fab 298 HC and Fab 298 KC are shown in white, grey and tan, respectively. The RBD is colored as in (a). (**D**) Superposition of Fabs 46 (light pink) and 52 (dark pink) when bound to the RBD (green) reveals a distinct angle of approach for the two mAbs.

Fig. S8.



The MB platform potently overcomes SARS-CoV-2 sequence variability. (A) Comparison of the neutralization potency of selected IgGs and MBs against WT PsV (dark red) and the more infectious D614G PsV (grey). (B) Schematic representation of a tri-specific MB generated by combination of three Fab specificities and the Fc fragment using the MB split design. (C) Cocktails and tri-specific MBs that combine the specificities of mAbs 298, 80 and 52, or 298, 324 and 46 were generated and tested against WT PsV. (D) Neutralization potency change of cocktails and tri-specific MBs against pseudotyped SARS-CoV-2 variants in comparison to WT PsV. PsV variants that were sensitive to individual antibodies within the cocktails were selected. The area within the dotted lines represent a 3-fold change in IC_{50} value. This threshold was established as the cutoff to establish increased sensitivity (up bars) and increased resistance (down bars). (E) Neutralization titration curves showing three biological replicates of cocktails and tri-specific MBs against the authentic SARS-CoV-2/SB2-P4-PB strain⁴⁵. Mean IC_{50} values of three biological replicates are shown.

Table S2. Cryo-EM data collection and image processing

	Fab 80-Spike	Fab 298-Spike	Fab 324-Spike	Fab 46-RBD
EMDB ID	EMD-22739	EMD-22740	EMD-22741	EMD-22738
Data Collection				
Electron microscope	Titan Krios G3	Titan Krios G3	Titan Krios G3	Titan Krios G3
Camera	Falcon 4EC	Falcon 4EC	Falcon 4EC	Falcon 4EC
Voltage (kV)	300	300	300	300
Nominal magnification	75,000	75,000	75,000	75,000
Calibrated physical pixel size (Å)	1.03	1.03	1.03	1.03
Total exposure (e-/Å²)	44	44	44	44
Number of frames	29	29	29	29
Image Processing				
Motion correction software	<i>cryoSPARC v2</i> , <i>Relion MotionCorr</i>	<i>cryoSPARC v2</i> , <i>Relion MotionCorr</i>	<i>cryoSPARC v2</i> , <i>Relion MotionCorr</i>	<i>cryoSPARCv2</i>
CTF estimation software	<i>cryoSPARCv2</i>	<i>cryoSPARCv2</i>	<i>cryoSPARCv2</i>	<i>cryoSPARCv2</i>
Particle selection software	<i>cryoSPARCv2</i>	<i>cryoSPARCv2</i>	<i>cryoSPARCv2</i>	<i>cryoSPARCv2</i>
3D map classification and refinement software	<i>cryoSPARCv2</i>	<i>cryoSPARCv2</i>	<i>cryoSPARCv2</i>	<i>cisTEM</i>
Micrographs used (total)	3610	7772	4478	4722
0° tilt	820	4259	1098	4722
40° tilt	2790	3513	3380	0
Global resolution (Å)	6.2	6.2	6	4
Particles in final maps	7,525	26,972	18,595	32,283

Table S3. X-ray crystallography data collection and refinement statistics

Fab 52- Fab 298- SARS-CoV-2 RBD	
PDB ID	7K9Z
Data Collection	
Wavelength (Å)	1.03317
Space group	P 3 ₂ 2 1
Cell dimensions	
a,b,c (Å)	87.6, 87.6, 325.1
α, β, γ (°)	90.0, 90.0, 120.0
Resolution (Å)	39.66-2.95 (3.05-2.95)
No. Molecules in ASU	1
No. Total observations	496,550 (43,958)
No unique observations	31,545 (3,060)
Multiplicity	15.7 (14.3)
R _{merge} (%)	16.8 (74.2)
R _{pim} (%)	4.3 (20.1)
<I/σI>	12.3 (1.4)
CC _{1/2}	99.8 (86.3)
Completeness (%)	99.9 (99.9)
Refinement	
Non-hydrogen atoms	8061
Macromolecule	8047
Glycan	14
R _{work} /R _{free}	0.259/0.286
Rms deviations	
Bond lengths (Å)	0.002
Bond angles (°)	0.53
Ramachandran plot	
Favored regions (%)	95.6
Allowed regions (%)	4.1
Outliers (%)	0.3
Rotamer Outliers (%)	2.6
B-factors (Å ²)	
Wilson B-factor	78.6
Average B-factors	103.9
Average macromolecule	103.9
Average glycan	114.3

Table S4. RBD residues contacting Fab 298 identified by PISA (Krissinel and Henrick, 2007).

RBD	Residue	BSA (Å ²)	Interaction	Fab 298 (H-HC, K-KC)
453	Tyr	2	vdW	H-Thr31, H-Ile100
455	Leu	20	vdW	H-Thr31, H-Ile100
456	Phe	30	vdW	H-Thr31, H-Tyr32
458	Lys	1	vdW	K-Ser27F
474	Gln	12	vdW	K-Tyr27D
	Gln ^{NE2}		HB	K-Tyr27D ^{OH}
475	Ala	45	vdW	K-Tyr27D, H-Tyr32, K-Tyr32, H-Arg97
	Ala ^O		HB	K-Tyr32 ^{OH}
476	Gly	23	vdW	K-Tyr27D, K-Tyr32, K-Tyr91, K-Tyr92, K-Ser93, H-Arg97
477	Ser	75	vdW	K-Tyr27D, K-Tyr92, K-Ser93, K-Thr94
	Ser ^N		HB	K-Tyr92 ^O
	Ser ^{OG}		HB	K-Tyr92 ^O
478	Thr	41	vdW	K-Tyr27D, K-Tyr92, K-Ser93, K-Thr94
	Thr ^{OG1}		HB	K-Thr94 ^{OG1}
484	Glu	74	vdW	H-Trp50, H-Ser52, H-Ser54, H-Gly55, H-Gly56, H-Thr57, H-Asp58
	Glu ^{OE2}		HB	H-Ser54 ^{OG}
485	Gly	28	vdW	H-Trp50, H-Thr57, H-Asp58
486	Phe	169	vdW	K-Gln89, K-Tyr91, K-Ser93, K-Thr94, K-Pro96, H-Ser35, H-Trp47, H-Trp50, H-Asp58, H-Asp95, H-Arg97
	Phe ^N		HB	H-Asp58 ^{OD2}
	Phe ^O		HB	K-Thr94 ^{OG1}
487	Asn	41	vdW	K-Tyr32, K-Tyr91, K-Ser93, K-Thr94, H-Asp95, H-Arg97
	Asn ^{OD1}		HB	H-Arg97 ^{NH2}
	Asn ^{ND2}		HB	K-Tyr91 ^O , K-Tyr92 ^O
488	Cys	1	vdW	H-Trp50
489	Tyr	84	vdW	H-Ser30, H-Thr31, H-Tyr32, H-Trp50, H-Asp95, H-Arg97,
	Tyr ^{OH}		HB	H-Arg97 ^{NH2} , H-Asp95 ^{OD2}
493	Gln	45	vdW	H-Ser30, H-Thr31, H-Ile100
Total BSA (Å²):		691		

vdW: van der Waals interaction (5.0 Å cut-off)

HB: hydrogen bond (3.8 Å cut-off)

SB: salt bridge (4.0 Å cut-off)

Table S5. Fab 298 residues contacting RBD identified by PISA (Krissinel and Henrick, 2007).

Fab 298	Residue	Chain	BSA (Å ²)	Interaction	RBD
30	Ser	H	9	vdW	Tyr489, Gln493
31	Thr	H	68	vdW	Tyr453, Leu455, Phe456, Tyr489, Gln493
32	Tyr	H	57	vdW	Phe456, Ala475, Tyr489
35	Ser	H	8	vdW	Phe486
47	Trp	H	23	vdW	Phe486
50	Trp	H	79	vdW	Glu484, Gly485, Phe486, Cys488, Tyr489
52	Ser	H	8	vdW	Glu484
54	Ser	H	17	vdW	Glu484
	Ser ^{OG}			HB	Glu484 ^{OE2}
55	Gly	H	7	vdW	Glu484
56	Gly	H	7	vdW	Glu484
57	Thr	H	10	vdW	Glu484, Gly485
58	Asp	H	28	vdW	Glu484, Gly485, Phe486
	Asp ^{OD2}			HB	Phe486 ^N
95	Asp	H	15	vdW	Phe486, Asn487, Tyr489
	Asp ^{OD2}			HB	Tyr489 ^{OH}
97	Arg	H	61	vdW	Asn487, Tyr489
	Arg ^{NH2}			HB	Asn487 ^{OD1} , Tyr489 ^{OH}
100	Ile	H	7	vdW	Tyr453, Leu455, Gln493
27D	Tyr	K	59	vdW	Gln474, Ala475, Gly476, Ser477, Thr478
	Tyr ^{OH}			HB	Gln474 ^{NE2}
27F	Ser	K	1	vdW	Lys458
32	Tyr	K	28	vdW	Ala475, Gly476, Asn487
	Tyr ^{OH}			HB	Ala475 ^O
89	Gln	K	1	vdW	Phe486
91	Tyr	K	30	vdW	Gly476, Phe486, Asn487
	Tyr ^O			HB	Asn487 ^{ND2}
92	Tyr	K	40	vdW	Gly476, Ser477, Thr478
	Tyr ^O			HB	Asn487 ^{ND2}
	Tyr ^O			HB	Ser477 ^N , Ser477 ^{OG}
93	Ser	K	26	vdW	Gly476, Ser477, Thr478, Phe486, Ser487
94	Thr	K	57	vdW	Ser477, Thr478, Phe486, Asn487
	Thr ^{OG1}			HB	Thr478 ^{OG1} , Phe486 ^O
96	Pro	K	23	vdW	Phe486

Total BSA (Å²): 669

vdW: van der Waals interaction (5.0 Å cut-off)

HB: hydrogen bond (3.8 Å cut-off)

SB: salt bridge (4.0 Å cut-off)

Table S6. RBD residues contacting Fab 52 identified by PISA (Krissinel and Henrick, 2007).

RBD	Residue	BSA (Å ²)	Interaction	Fab 52 (H-HC, K-KC)
346	Arg	45	vdW	H-Gln64
351	Tyr	29	vdW	K-Phe94, H-Ile52, H-Thr56, H-Asn58
352	Ala	19	vdW	K-Gly93, K-Phe94
354	Asn	6	vdW	K-Phe94
355	Arg	36	vdW	K-Ser0, K-Gln27
	Arg ^O		HB	K-Ser0 ^{OG}
356	Lys	13	vdW	K-Ser0
357	Arg	66	vdW	K-Ser0, K-Gln27
	Arg ^N		HB	K-Ser0 ^{OG}
	Arg ^{NH2}		HB	K-Gln27 ^{OE1}
449	Tyr	13	vdW	H-Phe554, H-Thr56
450	Asn	38	vdW	H-Phe554, H-Thr56
452	Leu	47	vdW	H-Ile52, H-Phe554, H-Gly55, H-Thr56
462	Lys	1	vdW	K-Ser30
465	Glu	28	vdW	K-Ser30, K-Asn31, K-Asn32, K-Asn92
	Glu ^{OE2}		HB	K-Ser30 ^{OG}
466	Arg	70	vdW	K-Asn32, K-Asn92, K-93Gly, K-Phe94
	Arg ^O		HB	K-Asn32 ^{ND2}
	Arg ^{NH1}		HB	K-Asn92 ^O
467	Asp	12	vdW	K-Asn32, K-Asn92, H-Asp98
468	Ile	102	vdW	K-Asn32, K-Gly91, K-Asn92, K-93Gly, K-Phe94, K-Leu96, H-Arg96, H-Gly97, H-Asp98
469	Ser	37	vdW	K-Asn32, H-Arg96, H-Gly97, H-Asp98
	Ser ^{OG}		HB	H-Asp98 ^{OD1}
470	Thr	67	vdW	H-Ser31, H-Tyr32, H-Gly33, H-Ile52, H-Asp95, H-Arg96, H-Gly97, H-Asp98
	Thr ^{OG1}		HB	H-Gly97 ^N
471	Glu	39	vdW	H-Tyr32, H-Arg96, H-Gly97, H-Asp98
	Glu ^{OE1}		SB	H-Arg96 ^{NH2}
	Glu ^{OE2}		SB	H-Arg96 ^{NH2}
472	Ile	7	vdW	H-Ser31, H-Tyr32, H-Arg96
481	Asn	1	vdW	H-Tyr32
482	Gly	42	vdW	H-Ser31, H-Tyr32
	Gly ^O		HB	H-Tyr32 ^{OH}
483	Val	12	vdW	H-Thr28, H-Ser31, H-Tyr32
484	Glu	53	vdW	H-Thr28, H-Phe29, H-Thr30, H-Ser31, H-Met54
490	Phe	87	vdW	H-Thr30, H-Ser31, H-Tyr32, H-Gly33, H-Ile52, H-Met54, H-Phe554
492	Leu	13	vdW	H-Ile52, H-Met54, H-Phe554
493	Gln	8	vdW	H-Phe554

494	Ser	17	vdW	H-Phe554
Total BSA (Å²):	904			

vdW: van der Waals interaction (5.0 Å cut-off)

HB: hydrogen bond (3.8 Å cut-off)

SB: salt bridge (4.0 Å cut-off)

Table S7. Fab 52 residues contacting RBD identified by PISA (Krissinel and Henrick, 2007).

Fab 52	Residue	Chain	BSA (Å²)	Interaction	RBD
28	Thr	H	24	vdW	Val483, Glu484
30	Thr	H	3	vdW	Glu484, Phe490
31	Ser	H	66	vdW	Glu471,Gly482,Val483, Glu484, Phe490
32	Tyr	H	51	vdW	Thr470, Glu471, Ile472, Asn481, Gly482, Val483, Phe490
	Tyr ^{OH}	H		HB	Gly482 ^O
33	Gly	H	7	vdW	Thr470, Phe490
52	Ile	H	62	vdW	Tyr351, Leu452, Thr470, Phe490, Leu492
53	Met	H	38	vdW	Glu484, Phe490, Leu492
54	Phe	H	110	vdW	Tyr449, Asn450, Leu452, Phe490, Leu492, Gln493, Ser494
55	Gly	H	4	vdW	Leu452
56	Thr	H	57	vdW	Tyr351, Tyr449, Asn450, Leu452
58	Asn	H	10	vdW	Tyr351
64	Gln	H	43	vdW	Arg346
95	Asp	H	2	vdW	Thr470
96	Arg	H	64	vdW	Ile468, Ser469, Thr470, Glu471, Ile472
	Arg ^{NH2}	H		SB	Glu471 ^{OE1} , Glu471 ^{OE2}
97	Gly	H	64	vdW	Ile468, Ser469, Thr470, Glu471
	Gly ^N			HB	Thr470 ^{OG1}
98	Asp	H	28	vdW	Asp467, Ile468, Ser469, Thr470, Glu471
	Asp ^{OD1}			HB	Ser469 ^{OG}
0	Ser	K	77	vdW	Arg355, Lys356, Arg357
	Ser ^{OG}			HB	Arg355 ^O , Arg357 ^N
27	Gln	K	60	vdW	Arg355, Arg357
	Gln ^{OE1}			HB	Arg357 ^{NH2}
30	Ser	K	28	vdW	Lys462, Glu465
	Ser ^{OG}			HB	Glu465 ^{OE2}
32	Asn	K	19	vdW	Glu465, Arg466, Asp467, Ile468, Ser469
	Asn ^{ND2}			HB	Arg466 ^O
91	Gly	K	18	vdW	Ile468
92	Asn	K	56	vdW	Glu465, Arg466, Asp467, Ile468
	Asn ^O			HB	Arg466 ^{NH1}
93	Gly	K	22	vdW	Ala352, Arg466, Ile468
94	Phe	K	56	vdW	Tyr351, Ala352, Asn354, Arg466, Ile468

96	Leu	K	5	vdW	Ile468
Total BSA (Å²):			974		

vdW: van der Waals interaction (5.0 Å cut-off)

HB: hydrogen bond (3.8 Å cut-off)

SB: salt bridge (4.0 Å cut-off)